Theoretical spectroscopy from the current density and the one-body Green's function

Arjan Berger

Contents

1 Curriculum Vitae **1**
- 1.1 Education . . . 1
- 1.2 Professional experience . . . 1
- 1.3 Awards . . . 1
- 1.4 Grants . . . 2
- 1.5 Advisor of Master, Ph.D. and post-doctoral students . . . 2
- 1.6 Invited Talks . . . 2
- 1.7 Contributed talks . . . 3
- 1.8 Organization of Conferences and Schools . . . 5
- 1.9 University teaching . . . 5
- 1.10 Publications . . . 6

2 Introduction **11**

3 Research activities **13**
- 3.1 An efficient *GW* calculation of quasi-particle energies: the effective-energy technique . . . 14
- 3.2 Fully parameter-free calculation of the optical spectra for insulators, semiconductors and metals from a simple polarization functional . . . 28
- 3.3 Gauge-Invariant Calculation of Static and Dynamical Magnetic Properties from the Current Density . . . 36
- 3.4 Unphysical and Physical Solutions in Many-Body Theories: from Weak to Strong Correlation . . . 45

4 Projects **51**
- 4.1 The magnetization of a periodic solid . . . 52
- 4.2 Topological phase prediction from the magneto-electric effect . . . 55
- 4.3 Theoretical description of resonant inelastic x-ray scattering . . . 58

Bibliography **60**

Chapter 1

Curriculum Vitae

1.1 Education

- *Ph.D.* in Chemistry, Rijksuniversiteit Groningen, Groningen, Netherlands (2006)
  Title : "Current-density-functionals for extended systems"
  Thesis advisor : Prof. Dr. R. Broer ; co-advisors: Dr. Ir. P.L. de Boeij, Dr. R. van Leeuwen

- *Master* in Chemistry (cum laude), Rijksuniversiteit Groningen, Groningen, The Netherlands (2002)
  Title :"Time-dependent current-density-functional theory for optical spectra; a study of the electric exchange-correlation field"
  Thesis advisor : Dr. Ir. P.L. de Boeij

1.2 Professional experience

- *Maître de conférences*, Laboratoire de Chimie et Physique Quantiques, IRSAMC, Université Toulouse III - Paul Sabatier, France (from Septembre 2011)

- *Postdoc*, Laboratoire des Solides Irradiés, Ecole Polytechnique, Palaiseau, France (April 2007-August 2011)

- *Postdoc*, Theoretical Chemistry Group, Rijksuniversiteit Groningen, Groningen, The Netherlands (September 2006-March 2007)

1.3 Awards

- Prime d'encadrement doctoral et de recherche (PEDR) (2016-2020)

- Chaire d'excellence CNRS (2011-2016)

1.4 Grants

- NEXT émergence (2017): 61000 Euro
- IDEX émergence (2015): 114000 Euro
- Chaire X-ESPCI-SAINT GOBAIN: 94056 Euro (2009)

1.5 Advisor of Master, Ph.D. and post-doctoral students

- Postdoc : Rubén Rodriguez Ferradás, Université Toulouse III - Paul Sabatier (from August 2016)
- Ph.D.: Stefano di Sabatino (Université Toulouse III - Paul Sabatier).
  Date of thesis defense: 5 November 2015.
- Ph.D.: Nathaniel Raimbault (Université Toulouse III - Paul Sabatier).
  Date of thesis defense: 4 November 2015.
- Master: Cyril Saussol, Université Toulouse III - Paul Sabatier (2015)
- Master: Thibault Ardhuin, Université Toulouse III - Paul Sabatier (2014)
- Master: Nicolas Trancart, Université Toulouse III - Paul Sabatier (2014)

1.6 Invited Talks

1. *Theoretical spectroscopy for molecules and solids from the current density.*
   Marseille Condensed Matter: Optics and magnetism, Marseille, France (2016).
2. *Theoretical spectroscopy for molecules and solids from the induced current density.*
   MAGIC-2016, Salerno, Italy (2016).
3. *Advances in Time-dependent Current-density-functional Theory.*
   16th International Conference Computational and mathematical methods in Science and Engineering, Rota, Spain (2016).

4. *Electric and Magnetic Response in BAND.*
   ADF developer workshop, Amsterdam, The Netherlands (2014).

5. *Polarization and Magnetization for Periodic Solids from Time-Dependent Current-DFT.*
   13th International Conference Computational and mathematical methods in Science and Engineering, Almeria, Spain (2013).

6. *Time-dependent current-density-functional theory for extended systems.*
   Theory days on current-density functional theory, Toulouse, France (2012).

7. *The effective-energy technique: GW calculations without summing over empty states.*
   Challenges and solutions in *GW* calculations for complex systems, Lausanne, Switzerland (2011).

8. *The effective-energy technique: GW calculations without summing over empty states.*
   5th international Abinit developer workshop, Han-sur-Lesse, Belgium (2011).

9. *Ab initio calculations of electronic excitations: Collapsing spectral sums.*
   15th International workshop on computational physics and materials science: total energy and force methods, Trieste, Italy (2011).

10. *The absorption of SnO_2 in the visible range.*
    Moving theory to applications, Palaiseau, France (2010).

11. *Theory and applications of time-dependent current-density-functional theory.*
    7th ETSF young researchers meeting, Jyväskylä, Finland (2010).

1.7 Contributed talks

1. *Fully parameter-free calculation of optical spectra for insulators, semiconductors and metals from a simple polarization functional.*
   CMD26, Groningen, Netherlands (2016).

2. *Advances in Time-dependent Current-density-functional Theory.*
   Réunion GDR-REST, Roscoff, France (2016).

3. *Advances in Time-dependent Current-density-functional Theory.*
   APS March meeting, Baltimore, USA (2016).

4. *Fully parameter-free calculation of optical spectra for insulators, semiconductors and metals from a simple polarization functional*
   Réunion GDR-CORREL, Marseille, France (2015).

5. *Fully parameter-free calculation of optical spectra for insulators, semiconductors and metals from a simple polarization functional*
   DPG Frühjarstagung, Berlin, Germany (2015).

6. *Fully parameter-free calculation of optical spectra for insulators, semiconductors and metals from a simple polarization functional*
   APS March meeting, San Antonio, USA (2015).

7. *The exact solution of the many-body problem in one point: insights in approximate Green's function approaches.*
   APS March meeting, Denver, USA (2014).

8. *The magnetization of periodic solids from time-dependent current-DFT.*
   APS March meeting, Baltimore, USA (2013).

9. *The magnetization of periodic solids from time-dependent current-DFT.*
   DPG Frühjarstagung, Regensburg, Germany (2013).

10. *Efficient GW calculations for SnO2, ZnO and rubrene: the effective-energy technique.*
    International Symposium and Workshop on Electron Correlations and Materials Properties of Compounds and Alloys, Porto Heli, Greece (2012).

11. *Efficient GW calculations for SnO2, ZnO and rubrene: the effective-energy technique.*
    International conference of advanced materials modeling, Nantes, France (2012).

12. *Ab initio calculations of electronic excitations: Collapsing spectral sums.*
    DPG Tagungen, Dresden, Germany (2011).

13. *Ab initio calculations of electronic excitations: Collapsing spectral sums.*
    ETSF workshop on electronic excitations, Berlin, Germany (2010).

14. *Ab initio calculations of electronic excitations: Collapsing spectral sums.*
    Psi-k 2010, Berlin, Germany (2010).

15. *Ab initio calculations of electronic excitations: Collapsing spectral sums.*
    International conference of advanced materials modeling, Nantes, France (2010).

16. *GW without empty states.*
    APS March meeting, Portland, United States (2010).

17. *GW without empty states.*
    13th ETSF workshop on electronic excitations, Evora, Portugal (2009).

18. *Real-time propagation in the time-dependent optimized-potential method.*
    4th Nanoquanta young researchers meeting, San Sebastian, Spain (2007).

19. *Time-dependent current-density-functional theory in extended systems.* Spectroscopy and theoretical chemistry meeting, NWO workshop, Lunteren, The Netherlands (2006).

20. *Ultranonlocal exchange-correlation effects in the response of extended systems.* The scientific FOM-days on condensed matter, Veldhoven, The Netherlands (2003).

1.8 Organization of Conferences and Schools

1. Luchon Tutorial in Theoretical Chemistry (LTTC) in Superbagnères de Luchon, France (2017)

2. CMD26 Colloquium: Theoretical spectroscopy: extending the *ab-initio* landscape in Groningen, Netherlands (2016)

3. Mini-workshop on multiple solutions in many-body theories in Paris, France (2016)

4. Luchon Tutorial in Theoretical Chemistry (LTTC) in Saint-Lary-Soulan, France (2016)

5. CECAM workshop: Green's function methods: the next generation II in Lausanne, Switzerland (2015)

6. Luchon Tutorial in Theoretical Chemistry (LTTC) in Superbagnères de Luchon, France (2015)

7. Theory days on self-interaction correction in Toulouse, France (2014)

8. CECAM workshop: Green's function methods: the next generation in Toulouse, France (2013)

1.9 University teaching

1. Density functional theory (Master) - lectures + practicum (2016–2017)

2. Numerical practicum (Bachelor) - practicum (2016–2017)

3. Light and color (Bachelor) - exercice classes (2016–2017)

4. Solid-state chemistry (Bachelor) - exercice classes (2016–2017)

5. Fundamentals of chemistry (Bachelor) - exercice classes (2016–2017)

6. Many-body perturbation theory (Graduate course) - lectures (2014–2015)
7. Thermodynamics (Bachelor) - lectures + exercice classes (2012–2016)
8. Optics (Bachelor) - exercice classes (2012–2016)
9. Applied mathematics (Bachelor) - exercice classes (2011–2014)
10. Quantum chemistry (Bachelor) - lectures + exercice classes (2011–2017)
11. Chemical bonding (Bachelor) - exercise class (2002–2005)

1.10 Publications

1. *The self-consistent Dyson equation and self-energy functionals: failure or new opportunities?*
   W. Tarantino, P. Romaniello, J. A. Berger, and L. Reining,
   Subbmitted to Phys. Rev. B; arXiv:1703.05587 (2017).

2. *Optical properties of periodic systems within the current-current response framework: pitfalls and remedies.*
   D. Sangalli, J. A. Berger, C. Attaccalite, M. Grüning, and P. Romaniello,
   Phys. Rev. B **95** 155203 (2017)

3. *Photoemission spectra from reduced density matrices: the band gap in strongly correlated systems*
   S. Di Sabatino, J. A. Berger, L. Reining, and P. Romaniello,
   Phys. Rev. B **94**, 155141 (2016)

4. *Gauge-invariant Formulation of Circular Dichroism*
   N. Raimbault, P. L. de Boeij, P. Romaniello, and J. A. Berger
   J. Chem. Theory Comput. **12**, 3278 (2016)

5. *Fully parameter-free calculation of optical spectra for insulators, semiconductors and metals from a simple polarization functional*
   J. A. Berger
   Phys. Rev. Lett. **115**, 137402 (2015)

6. *Unphysical and Physical Solutions in Many-Body Theories: from Weak to Strong Correlation* A. Stan, P. Romaniello, S. Rigamonti, L. Reining, and J. A. Berger
New J. Phys. **17**, 093045 (2015)

7. *Gauge-Invariant Calculation of Static and Dynamical Magnetic Properties from the Current Density*
N. Raimbault, P. L. de Boeij, P. Romaniello, and J. A. Berger
Phys. Rev. Lett. **114**, 066404 (2015)

8. *Reduced Density-Matrix Functional Theory: correlation and spectroscopy*
S. Di Sabatino, J. A. Berger, L. Reining, and P. Romaniello,
J. Chem. Phys. **143**, 024108 (2015)

9. *Solution to the many-body problem in one point*
J. A. Berger, P. Romaniello, F. Tandetzky, B. Mendoza, C. Brouder, and L. Reining
New J. Phys. **16**, 113025 (2014)

10. *A rational reduction of CI expansions: combining localized molecular orbitals and selected charge excitations*
T. Krah, N. Ben Amor, D. Maynau, J. A. Berger, and V. Robert
J. Mol. Mod. **20**, 2240 (2014)

11. *Efficient calculation of the polarizability: a simplified effective-energy technique*
J. A. Berger, L. Reining, and F. Sottile
Eur. Phys. J. B **85**, 326 (2012)

12. *Efficient GW calculations for SnO_2, ZnO, and rubrene: The effective-energy technique*
J. A. Berger, L. Reining, and F. Sottile
Phys. Rev. B **85**, 085126 (2012)

13. *Ab initio calculations of electronic excitations: Collapsing spectral sums.*
J. A. Berger, L. Reining, and F. Sottile
Phys. Rev. B **82**, 041103(R) (2010).

14. *Double excitations in finite systems.*
P. Romaniello, D. Sangalli, J. A. Berger, F. Sottile, L. Molinari, L. Reining, G.

Onida, J.
J. Chem. Phys. **130**, 044108 (2009).

15. *Analysis of the Vignale-Kohn current functional in the calculation of optical spectra.*
J. A. Berger, P. L. de Boeij, and R. van Leeuwen.
Phys. Rev. B **75**, 035116 (2007).

16. *Performance of the Vignale-Kohn functional in the linear response of metals.*
J. A. Berger, P. Romaniello, R. van Leeuwen, and P. L. de Boeij.
Phys. Rev. B **74**, 245117 (2006).

17. *A physical model for the longitudinal polarizabilities of polymer chains.*
J. A. Berger, P. L. de Boeij, and R. van Leeuwen.
J. Chem. Phys. **123**, 174910 (2005).

18. *Analysis of the viscoelastic coefficients in the Vignale-Kohn functional: The cases of one- and three-dimensional polyacetylene.*
J. A. Berger, P. L. de Boeij, and R. van Leeuwen.
Phys. Rev. B **71**, 155104 (2005).

19. *Size-scaling of the polarizability of tubular fullerenes investigated with time-dependent (current)-density-functional theory.*
M. van Faassen, L. Jensen, J. A. Berger, and P. L. de Boeij.
Chem. Phys. Lett. **395**, 274 (2004).

20. *Application of time-dependent current-density-functional theory to nonlocal exchange-correlation effects in polymers.*
M. van Faassen, P. L. de Boeij, R. van Leeuwen, J. A. Berger, and J. G. Snijders.
J. Chem. Phys. **118**, 1044 (2003).

21. *Ultranonlocality in time-dependent current-density-functional theory: Applications to conjugated polymers.*
M. van Faassen, P. L. de Boeij, R. van Leeuwen, J. A. Berger, and J. G. Snijders.
Phys. Rev. Lett. **88**, 186401 (2002).

22. *Current-density-functional theory for optical spectra: A successful polarization functional.*
P. L. de Boeij, F. Kootstra, J. A. Berger, R. van Leeuwen, and J. G. Snijders.
J. Chem. Phys. **115**, 1995 (2001).

Chapter 2

Introduction

The work described in this manuscript focuses on theory and method developments in the framework of *ab initio* theoretical spectroscopy, *i.e.*, numerical experiments giving spectroscopic data, e.g., band structures, optical absorption and circular dichroism, without using empirical or adjustable parameters. These data contain valuable information about the system under study and, therefore, a first-principles description of these spectroscopies is important for the interpretation, analysis and, ultimately, the prediction of experiments. To obtain the spectroscopic data we will use the current density and the one-body Green's function as the fundamental variables. This requires some explanation.

As is well known, when doing numerical experiments there is a trade-off between the numerical efficiency and the accuracy of a given theory or method. At the far end of one side we have full configuration interaction (FCI) which is accurate but numerically expensive, and at the far end on the other side we have density-functional theory (DFT), which is numerically efficient but not always very accurate. Both theories give, in principle, access to all observables. For FCI this is obvious since it yields the many-body wave function while for DFT this is guaranteed by the Hohenberg-Kohn theorem [1]. Here we are interested in developing theory and methodology that can be applied to systems that contain a large number of electrons and, therefore, we have to focus on the DFT side of the spectrum. So why not use DFT to calculate band structures, optical absorption and circular dichroism? Besides numerical efficiency and accuracy there are other aspects that should be taken into consideration:

1. *The difficulty to extract the desired information from the theory*
   Let us consider the band structure of a solid, *i.e.*, the electron removal and addition energies. This information is in principle contained in the ground-state density, thanks to the Hohenberg-Kohn theorem, but there is no known procedure that tells us how to extract the band structure from the ground-state density. In other words, there is no knonwn functional that takes as input the ground-state density and yields the band structure. Instead, the band structure can be easily deduced from the one-body Green's function since its poles are the

electron removal and addition energies. Therefore, despite the fact that Green's function methods are numerically more expensive than DFT, it is the method of choice for the calculation of band structures.

2. *Extended systems described by periodic boundary conditions*
   For extended systems such as solids it is useful to model them with periodic boundary conditions in order to avoid the explicit treatment of $\sim 10^{23}$ electrons. However, as a consequence one has only the knowledge of the density in the bulk of the material but not of the density at the surface. It turns out that the bulk density is not sufficient to fully characterize the system. In particular, the induced polarization of such a system due to an electric field is not a functional of the bulk density alone [2]. However, the induced polarization due to an electric field is a functional of the current density in the bulk.

3. *Magnetic fields*
   Whenever a transverse vector potential is present in the Hamiltonian, for example in the case of a magnetic field, the Hohenberg-Kohn theorem as well as its extension to time-dependent systems [3] do not apply. However, generalizations of these theorems can be derived when one switches from the density to the current density as the fundamental variable [4–7].

For these reasons we choose to work with the one-body Green's function and the current density, instead of the density.

The manuscript is organized as follows. In chapter 3 I will give an overview of my main research activities. In section 3.1 I will describe how one can efficiently calculate quasi-particle energies. These energies give important information about the band structure but can also be used to build response functions from which one can calculate response properties, such as optical absorption spectra. In section 3.2 I will show how, using a simple polarization functional, one can obtain accurate optical spectra. While optical absorption can be described as a response to a perturbing electric field, I will discuss how one can treat response properties of molecules that have a magnetic component in section 3.3. Finally, in section 3.4 I will discuss the problem of multiple solutions when solving nonlinear equations in many-body theories. In chapter 4 we will present an outlook of future projects. The project described in section 4.1 aims to find a general many-body description of the magnetization that is compatible with periodic boundary conditions. The goal of the project in section 4.2 is to predict topological phases from the magneto-electric polarizability. Finally, the project detailed in section 4.3 will provide the theory and a numerical tool to do resonant inelastic x-ray spectroscopy (RIXS).

Chapter 3

Research activities

In this chapter I will give an overview of my main research activities. In order to focus on the main ideas and not get lost in details I will not discuss many characteristics related to implementation and computation. This information can be found in the original papers which are cited at the beginning of each section. I will also not describe in much detail the underlying theories that are used, *i.e.*, density-functional theory, time-dependent current-density-functional theory and many-body perturbation theory, since explanations of these methods can be found in many excellent books and articles. In summary, the goal of this chapter is to highlight the improvements brought about by my research with respect to standard theories and methodologies.

3.1 An efficient GW calculation of quasi-particle energies: the effective-energy technique

In this section we will discuss the effective-energy technique, a method we developed to improve the numerical efficiency of the calculation of GW quasi-particle energies by reducing or even avoiding completely the summation over empty states in the calculation of the independent-particle polarizability and the GW self-energy. Here we summarize the main results of the effective-energy technique. In the following we will mainly focus on standard perturbative GW, also called one-shot GW, or G^0W^0. For the details of the G^0W^0 method we refer the reader to excellent review articles such as the one in Ref. [8]. Here we will focus only on the two aspects that are different in our approach with respect to the standard G^0W^0 approach, i.e., the calculation of the polarizability and the correlation part of the self-energy.

corresponding publications:

- *Ab initio calculations of electronic excitations: Collapsing spectral sums.*
  J. A. Berger, L. Reining, and F. Sottile
  Phys. Rev. B **82**, 041103(R) (2010).

- *Efficient GW calculations for SnO_2, ZnO, and rubrene: The effective-energy technique*
  J. A. Berger, L. Reining, and F. Sottile
  Phys. Rev. B **85**, 085126 (2012)

- *Efficient calculation of the polarizability: a simplified effective-energy technique*
  J. A. Berger, L. Reining, and F. Sottile
  Eur. Phys. J. B **85**, 326 (2012)

Within many-body perturbation theory, all many-body effects are contained in the self-energy which, in practice, we approximate. The GW approximation for the self-energy proposed by Hedin [9] has become the standard tool for the calculation of quasiparticle energies. In the GW approximation the electrons do not interact via the Coulomb interaction, as, for example, in Hartree-Fock, but via the dynamically screened Coulomb interaction W. The physical motivation is that in many-body systems (solids, clusters, macromolecules) the electron-electron repulsion is, in general, strong, such that each electron is surrounded by a Coulomb hole of positive charge, *i.e.*, the positive nuclear charge is not completely canceled. For this reason it is more physical to consider the interaction between quasi-particles composed of electrons and their Coulomb holes. Since the interaction between quasi-particles is much weaker than between electrons, thanks to the Coulomb hole which screens each electron from the other electrons, an expansion in terms of W converges more rapidly. The first

order term in such an expansion leads to the GW approximation in which the self-energy is just a product of the one-body Green's function G and W. The amount of screening depends on how polarizable the system is. Therefore, in practice, we calculate the polarizability to construct W. The GW method has been very successful in the calculation of band gaps and band structures of many systems. However, the main disadvantage of GW is that it is numerically expensive. This is mainly due to the large number of empty states that must be taken into account in the standard spectral representations of the self-energy and the polarizability.

To illustrate how we can overcome this problem we will focus on the polarizability. Within G^0W^0 one calculates the time-ordered independent-particle polarizability. It is usually calculated as a sum over states (SOS) according to

$$\chi^0_{\vec{G}\vec{G}'}(\vec{q},\omega) = \sum_{s=\pm 1}\sum_{v,c} \frac{\tilde{\rho}^*_{cv}(\vec{q}+\vec{G})\tilde{\rho}_{cv}(\vec{q}+\vec{G}')}{s\omega - (\varepsilon_c - \varepsilon_v) + i\eta},, \tag{3.1}$$

where $\tilde{\rho}_{cv}(\vec{q}+\vec{G}) = \langle c|e^{-i(\vec{q}+\vec{G})\cdot\vec{r}}|v\rangle$, $|v\rangle$ ($|c\rangle$) and ε_v (ε_c) are valence (conduction) states and energies, respectively, $\vec{G}$ and $\vec{G}'$ are reciprocal lattice vectors, $\vec{q}$ is a vector that lies within the first Brillouin zone, and η is an infinitesimal. In practice, we obtain the states and energies within the local-density approximation (LDA) of density-functional theory (DFT). We note that the summation over s in the above equation is just a concise way to include both the resonant and anti-resonant contributions. Since here we focus on extended systems described by periodic boundary condition the indices v and c in the above expression should be considered multi-indices composed of the band index, the spin and the Bloch vector.

To eliminate the summation over the empty states we now introduce a dynamical effective energy $\delta_v(\omega)$ that takes into account the contribution of all the empty states to the polarizability. This idea is illustrated in Fig. 3.1 where, for each valence band, the ensemble of the empty bands is replaced by a single band $\delta_v(\omega)$. The effective energy $\delta_{v\vec{G}\vec{G}'}(\vec{q},\omega)$ takes into account the contributions of all the empty states to $\chi_0(\omega)$. This change can be done exactly according to

$$\chi^0_{\vec{G}\vec{G}'}(\vec{q},\omega) = \sum_{s=\pm 1}\sum_{v,c} \frac{\tilde{\rho}^*_{cv}(\vec{q}+\vec{G})\tilde{\rho}_{cv}(\vec{q}+\vec{G}')}{s\omega^+ - (\delta_{v\vec{G}\vec{G}'}(\vec{q},s\omega^+) - \epsilon_v)}, \tag{3.2}$$

where $s\omega^+ = s\omega + i\eta$. We can now use the closure relation, $\sum_c |c\rangle\langle c| = 1 - \sum_v |v\rangle\langle v|$ to obtain an expression that contains a summation over occupied states only:

$$\chi^0_{\vec{G}\vec{G}'}(\vec{q},\omega) = \sum_{s=\pm 1}\sum_{v} \frac{f^{\rho\rho}_{v\vec{G}\vec{G}'}(\vec{q})}{s\omega^+ - (\delta_{v\vec{G}\vec{G}'}(\vec{q},s\omega^+) - \epsilon_v)}, \tag{3.3}$$

where we defined, for a general state n,

$$f^{\rho\rho}_{n\vec{G}\vec{G}'}(\vec{q}) = \tilde{\rho}_{nn}(\vec{G}'-\vec{G}) - \sum_v \tilde{\rho}^*_{vn}(\vec{q}+\vec{G})\tilde{\rho}_{vn}(\vec{q}+\vec{G}'). \tag{3.4}$$

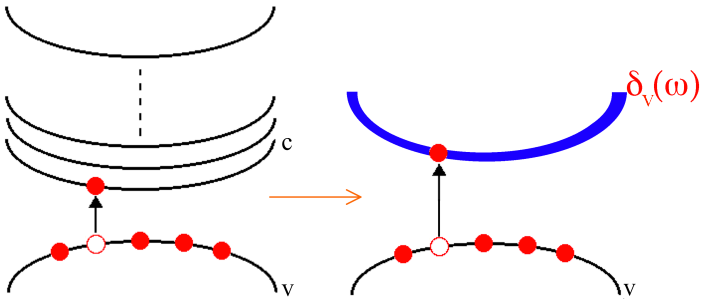

Figure 3.1: Within the EET applied to the polarizability, for each valence state v, the ensemble of conductions states c is replaced by single frequency-dependent effective energy $\delta_v(\omega)$. Therefore, instead of an infinite number of transitions contributing to the polarizability for each valence state, within the EET only one transition contributes.

It now remains to find accurate approximations to $\delta_v(\omega)$. By comparing the summations over the empty states contained in Eqs. (3.1) and (3.2) we arrive at the following implicit equation for $\delta_v(\omega)$,

$$\sum_c \frac{\tilde{\rho}^*_{cv}(\vec{q}+\vec{G})\tilde{\rho}_{cv}(\vec{q}+\vec{G}')}{s\omega^+ - (\varepsilon_c - \varepsilon_v)} = \sum_c \frac{\tilde{\rho}^*_{cv}(\vec{q}+\vec{G})\tilde{\rho}_{cv}(\vec{q}+\vec{G}')}{s\omega^+ - (\delta_{v\vec{G}\vec{G}'}(\vec{q}, s\omega^+) - \varepsilon_v)}. \tag{3.5}$$

Subtracting the right-hand side from both sides we obtain

$$\sum_c \tilde{\rho}^*_{cv}(\vec{q}+\vec{G})\tilde{\rho}_{cv}(\vec{q}+\vec{G}') \left[\frac{(\varepsilon_c - \delta_{v\vec{G}\vec{G}'}(\vec{q}, s\omega^+))}{[s\omega^+ - (\varepsilon_c - \varepsilon_v)][s\omega^+ - (\delta_{v\vec{G}\vec{G}'}(\vec{q}, s\omega^+) - \varepsilon_v)]}\right] = 0. \tag{3.6}$$

Multiplying the above equation by $s\omega^+ - (\delta_{v\vec{G}\vec{G}'}(\vec{q}, s\omega^+) - \varepsilon_v)$ and rearranging we arrive at

$$\sum_c \frac{\varepsilon_c\tilde{\rho}^*_{cv}(\vec{q}+\vec{G})\tilde{\rho}_{cv}(\vec{q}+\vec{G}')}{[s\omega^+ - (\varepsilon_c - \varepsilon_v)]} - \delta_{v\vec{G}\vec{G}'}(\vec{q}, s\omega^+) \sum_c \frac{\tilde{\rho}^*_{cv}(\vec{q}+\vec{G})\tilde{\rho}_{cv}(\vec{q}+\vec{G}')}{[s\omega^+ - (\varepsilon_c - \varepsilon_v)]} = 0. \tag{3.7}$$

We can therefore rewrite the effective energy exactly as

$$\delta_{v\vec{G}\vec{G}'}(\vec{q}, s\omega^+) = \sum_c \frac{\varepsilon_c\tilde{\rho}^*_{cv}(\vec{q}+\vec{G})\tilde{\rho}_{cv}(\vec{q}+\vec{G}')}{[s\omega^+ - (\varepsilon_c - \varepsilon_v)]} \Bigg/ \sum_c \frac{\tilde{\rho}^*_{cv}(\vec{q}+\vec{G})\tilde{\rho}_{cv}(\vec{q}+\vec{G}')}{[s\omega^+ - (\varepsilon_c - \varepsilon_v)]}. \tag{3.8}$$

This exact expression is not useful in practice because it still has summations over the empty states. However, by using the fact that ϵ_c and $|c\rangle$ are the eigenvalue and eigenstate, respectively, of a corresponding Hamiltonian $\hat{H}$, we can rewrite the numerator on the right-hand side and obtain

$$\begin{aligned}\delta_{v\vec{G}\vec{G}'}(\vec{q}, s\omega^+) &= \varepsilon_v \\ &+ \frac{1}{2}\sum_c \frac{\tilde{\rho}^*_{cv}(\vec{q}+\vec{G})\langle c|[\hat{H}(\vec{r}), e^{-i(\vec{q}+\vec{G}')\cdot\vec{r}}]|v\rangle + h.c.}{[s\omega^+ - (\varepsilon_c - \varepsilon_v)]} \Bigg/ \sum_c \frac{\tilde{\rho}^*_{cv}(\vec{q}+\vec{G})\tilde{\rho}_{cv}(\vec{q}+\vec{G}')}{[s\omega^+ - (\varepsilon_c - \varepsilon_v)]},\end{aligned} \tag{3.9}$$

where *h.c.* denotes the Hermitian conjugate. This symmetrization is done because the commutator can be taken equally well in $\tilde{\rho}_{cv}$ as in $\tilde{\rho}^*_{cv}$. It will ensure that approximations to $\delta_{v\vec{G}\vec{G}'}$ derived below will have the correct symmetry, *i.e.*, $\delta_{v\vec{G}\vec{G}'}(\vec{q}, s\omega^+) = \delta^*_{v\vec{G}'\vec{G}}(\vec{q}, s\omega^+)$, which holds for the exact effective energy, as can be seen from Eq. (3.8). Here we will consider a Hamiltonian that contains only a local potential, *i.e.*, $\hat{H}(\vec{r}) = -\nabla^2_{\vec{r}}/2 + v(\vec{r})$. The derivation that follows can be easily generalized to include Hamiltonians with additional nonlocal potentials. Working out the commutator we obtain

$$\delta_{v\vec{G}\vec{G}'}(\vec{q}, s\omega^+) = \varepsilon_v + \frac{1}{2}\left[\frac{|\vec{q}+\vec{G}|^2}{2} + \frac{|\vec{q}+\vec{G}'|^2}{2}\right] + \frac{1}{2}\sum_c \frac{\tilde{\rho}^*_{cv}(\vec{q}+\vec{G})\tilde{j}_{cv}(\vec{q}+\vec{G}') + h.c.}{[s\omega^+ - (\varepsilon_c - \varepsilon_v)]} \Big/ \sum_c \frac{\tilde{\rho}^*_{cv}(\vec{q}+\vec{G})\tilde{\rho}_{cv}(\vec{q}+\vec{G}')}{[s\omega^+ - (\varepsilon_c - \varepsilon_v)]}, \tag{3.10}$$

where we defined

$$\tilde{j}_{cn}(\vec{q}+\vec{G}) = \langle c|e^{-i(\vec{q}+\vec{G})\cdot\vec{r}}[i\nabla_{\vec{r}}]|n\rangle \cdot (\vec{q}+\vec{G}). \tag{3.11}$$

The above expression is exact but still contains summations over empty states. However, one can obtain an approximate effective energy that is independent of empty states by neglecting the last term on the right-hand side. Plugging this simple frequency-independent approximation into Eq. (3.3) we obtain

$$\chi^0_{\vec{G}\vec{G}'}(\vec{q}, \omega) \approx \sum_{s=\pm 1}\sum_v \frac{f^{\rho\rho}_{v\vec{G}\vec{G}'}(\vec{q})}{s\omega^+ - \frac{1}{2}\left[\frac{|\vec{q}+\vec{G}|^2}{2} + \frac{|\vec{q}+\vec{G}'|^2}{2}\right]} \tag{3.12}$$

The above approximation has only a single pole and will therefore not be a good approximation to the true $\chi^0_{\vec{G}\vec{G}'}(\vec{q}, \omega)$ which has a number of poles equal to $N_v N_c$ where N_v (N_c) is the number of valence (conduction) states. However, the *GW* self-energy is a frequency integral over $\chi^0_{\vec{G}\vec{G}'}(\vec{q}, \omega)$ and therefore, the crude approximation in Eq. (3.12) might still give accurate quasi-particle energies if the position of its unique pole is a good average of the poles of the exact $\chi^0_{\vec{G}\vec{G}'}(\vec{q}, \omega)$. However, this is not guaranteed and therefore we will now try to improve over this simple approximation.

Comparing the numerator in Eq. (3.10) to the left-hand side of Eq. (3.5) we see that the two expressions have a very similar structure. This suggests that we can introduce a second effective energy $\tilde{\delta}_v(\omega)$ implicitly defined by

$$\sum_c \frac{\tilde{\rho}^*_{cv}(\vec{q}+\vec{G})\tilde{j}_{cv}(\vec{q}+\vec{G}')}{s\omega^+ - (\varepsilon_c - \varepsilon_v)} = \sum_c \frac{\tilde{\rho}^*_{cv}(\vec{q}+\vec{G})\tilde{j}_{cv}(\vec{q}+\vec{G}')}{s\omega^+ - (\tilde{\delta}_{v\vec{G}\vec{G}'}(\vec{q}, s\omega^+) - \varepsilon_v)} \tag{3.13}$$

which allows us to rewrite Eq. (3.10) as

$$\delta_{v\vec{G}\vec{G}'}(\vec{q},s\omega^+) = \varepsilon_v + \frac{1}{2}\left[\frac{|\vec{q}+\vec{G}|^2}{2}+\frac{|\vec{q}+\vec{G}'|^2}{2}\right] + \frac{1}{2}\sum_c \frac{\tilde{\rho}^*_{cv}(\vec{q}+\vec{G})\tilde{j}_{cv}(\vec{q}+\vec{G}')+h.c.}{[s\omega^+-(\tilde{\delta}_{v\vec{G}\vec{G}'}(\vec{q},s\omega^+)-\varepsilon_v)]}\Big/\sum_c \frac{\tilde{\rho}^*_{cv}(\vec{q}+\vec{G})\tilde{\rho}_{cv}(\vec{q}+\vec{G}')}{[s\omega^+-(\varepsilon_c-\varepsilon_v)]} \tag{3.14}$$

$$= \varepsilon_v + \frac{1}{2}\left[\frac{|\vec{q}+\vec{G}|^2}{2}+\frac{|\vec{q}+\vec{G}'|^2}{2}\right] + \frac{f^{\rho j}_{v\vec{G}\vec{G}'}(\vec{q})}{f^{\rho\rho}_{v\vec{G}\vec{G}'}(\vec{q})}\frac{s\omega^+-(\delta_{v\vec{G}\vec{G}'}(\vec{q},s\omega^+)-\varepsilon_v)}{s\omega^+-(\tilde{\delta}_{v\vec{G}\vec{G}'}(\vec{q},s\omega^+)-\varepsilon_v)} \tag{3.15}$$

where in the last step we used Eq. (3.5) and we defined

$$f^{\rho j}_{n\vec{G}\vec{G}'}(\vec{q}) = \frac{1}{2}\left[-\sum_v \tilde{\rho}^*_{vn}(\vec{q}+\vec{G})\tilde{j}_{vn}(\vec{q}+\vec{G}')+\langle n|e^{i(\vec{G}-\vec{G}')\cdot\vec{r}}(i\nabla)|n\rangle\cdot(\vec{q}+\vec{G}')\right]+h.c. \tag{3.16}$$

The above expression is exact but cannot be used since $\tilde{\delta}_v(\omega)$ is unknown. However, it can be used to obtain an approximation for $\delta_v(\omega)$. It can be proved that for a homogeneous electron gas $\delta_v(\omega)=\tilde{\delta}_v(\omega)$ [10], in which case the last division on the right-hand side of Eq. (3.15) becomes the identity. This suggests the following approximation

$$\delta_{v\vec{G}\vec{G}'}(\vec{q},s\omega^+) \approx \varepsilon_v + \frac{1}{2}\left[\frac{|\vec{q}+\vec{G}|^2}{2}+\frac{|\vec{q}+\vec{G}'|^2}{2}\right] + \frac{f^{\rho j}_{v\vec{G}\vec{G}'}(\vec{q})}{f^{\rho\rho}_{v\vec{G}\vec{G}'}(\vec{q})}. \tag{3.17}$$

which again is frequency independent. It leads to the following approximation for the polarizability

$$\chi^0_{\vec{G}\vec{G}'}(\vec{q},\omega) \approx \sum_{s=\pm1}\sum_v \frac{f^{\rho\rho}_{v\vec{G}\vec{G}'}(\vec{q})}{s\omega^+-\frac{1}{2}\left[\frac{|\vec{q}+\vec{G}|^2}{2}+\frac{|\vec{q}+\vec{G}'|^2}{2}\right]-\frac{f^{\rho j}_{v\vec{G}\vec{G}'}(\vec{q})}{f^{\rho\rho}_{v\vec{G}\vec{G}'}(\vec{q})}}. \tag{3.18}$$

This approximation has N_v poles, still much less than the N_vN_c poles of the true $\chi^0_{\vec{G}\vec{G}'}(\vec{q},\omega)$. But the strategy applied for $\delta_v(\omega)$ can be continued. Without going into details we can follow similar steps as before for $\delta_v(\omega)$ to obtain an exact expression for $\tilde{\delta}_v(\omega)$ in terms of a third effective energy $\tilde{\tilde{\delta}}_v(\omega)$:

$$\tilde{\delta}_{v\vec{G}\vec{G}'}(\vec{q},s\omega^+) = \varepsilon_v + \frac{1}{2}\left[\frac{|\vec{q}+\vec{G}|^2}{2}+\frac{|\vec{q}+\vec{G}'|^2}{2}\right] + \frac{1}{2}\sum_c \frac{\tilde{j}^*_{cv}(\vec{q}+\vec{G})\tilde{j}_{cv}(\vec{q}+\vec{G}')}{[s\omega^+-(\varepsilon_c-\varepsilon_v)]}\Big/\sum_c \frac{\tilde{\rho}^*_{cv}(\vec{q}+\vec{G})\tilde{j}_{cv}(\vec{q}+\vec{G}')}{[s\omega^+-(\varepsilon_c-\varepsilon_v)]} \tag{3.19}$$

$$= \varepsilon_v + \frac{1}{2}\left[\frac{|\vec{q}+\vec{G}|^2}{2}+\frac{|\vec{q}+\vec{G}'|^2}{2}\right] + \frac{f^{jj}_{n\vec{G}\vec{G}'}(\vec{q})}{f^{\rho j}_{n\vec{G}\vec{G}'}(\vec{q})}\frac{s\omega^+-(\tilde{\delta}_{v\vec{G}\vec{G}'}(\vec{q},s\omega^+)-\varepsilon_v)}{s\omega^+-(\tilde{\tilde{\delta}}_{v\vec{G}\vec{G}'}(\vec{q},s\omega^+)-\varepsilon_v)}, \tag{3.20}$$

where we defined

$$f^{jj}_{n\vec{G}\vec{G}'}(\vec{q}) = -\sum_v \tilde{j}^*_{vn}(\vec{q}+\vec{G})\tilde{j}_{vn}(\vec{q}+\vec{G}')+(\vec{q}+\vec{G})\cdot\langle\nabla_{\vec{r}}n|e^{i(\vec{G}-\vec{G}')\cdot\vec{r}}|\nabla_{\vec{r}}n\rangle\cdot(\vec{q}+\vec{G}'). \quad (3.21)$$

Inserting this expression into Eq. (3.15) we obtain

$$\delta_{v\vec{G}\vec{G}'}(\vec{q}, s\omega^+) = \varepsilon_v + \frac{1}{2}\left[\frac{|\vec{q}+\vec{G}|^2}{2} + \frac{|\vec{q}+\vec{G}'|^2}{2}\right] \quad (3.22)$$

$$+ \frac{f^{\rho j}_{v\vec{G}\vec{G}'}(\vec{q})}{f^{\rho\rho}_{v\vec{G}\vec{G}'}(\vec{q})} \frac{s\omega^+ - \frac{1}{2}\left[\frac{|\vec{q}+\vec{G}|^2}{2} + \frac{|\vec{q}+\vec{G}'|^2}{2}\right] - \frac{f^{\rho j}_{v\vec{G}\vec{G}'}(\vec{q})}{f^{\rho\rho}_{v\vec{G}\vec{G}'}(\vec{q})} \frac{s\omega^+ - (\delta_{v\vec{G}\vec{G}'}(\vec{q}, s\omega^+) - \varepsilon_v)}{s\omega^+ - (\tilde{\delta}_{v\vec{G}\vec{G}'}(\vec{q}, s\omega^+) - \varepsilon_v)}}{s\omega^+ - \frac{1}{2}\left[\frac{|\vec{q}+\vec{G}|^2}{2} + \frac{|\vec{q}+\vec{G}'|^2}{2}\right] - \frac{f^{jj}_{v\vec{G}\vec{G}'}(\vec{q})}{f^{\rho j}_{v\vec{G}\vec{G}'}(\vec{q})} \frac{s\omega^+ - (\delta_{v\vec{G}\vec{G}'}(\vec{q}, s\omega^+) - \varepsilon_v)}{s\omega^+ - (\tilde{\delta}_{v\vec{G}\vec{G}'}(\vec{q}, s\omega^+) - \varepsilon_v)}}. \quad (3.23)$$

Since for a homogeneous electron gas $\delta_v(\omega) = \tilde{\delta}_v(\omega) = \tilde{\tilde{\delta}}_v(\omega)$ in which case the last division on the right-hand side becomes the identity. This suggests the following approximation,

$$\delta_{v\vec{G}\vec{G}'}(\vec{q}, s\omega^+) \approx \varepsilon_v + \frac{1}{2}\left[\frac{|\vec{q}+\vec{G}|^2}{2} + \frac{|\vec{q}+\vec{G}'|^2}{2}\right] \quad (3.24)$$

$$+ \frac{f^{\rho j}_{v\vec{G}\vec{G}'}(\vec{q})}{f^{\rho\rho}_{v\vec{G}\vec{G}'}(\vec{q})} \frac{s\omega^+ - \frac{1}{2}\left[\frac{|\vec{q}+\vec{G}|^2}{2} + \frac{|\vec{q}+\vec{G}'|^2}{2}\right] - \frac{f^{\rho j}_{v\vec{G}\vec{G}'}(\vec{q})}{f^{\rho\rho}_{v\vec{G}\vec{G}'}(\vec{q})}}{s\omega^+ - \frac{1}{2}\left[\frac{|\vec{q}+\vec{G}|^2}{2} + \frac{|\vec{q}+\vec{G}'|^2}{2}\right] - \frac{f^{jj}_{v\vec{G}\vec{G}'}(\vec{q})}{f^{\rho j}_{v\vec{G}\vec{G}'}(\vec{q})}}, \quad (3.25)$$

which is frequency dependent. The corresponding approximation for the polarizability is then

$$\chi^0_{\vec{G}\vec{G}'}(\vec{q}, \omega) \approx \sum_{s=\pm1}\sum_v \frac{f^{\rho\rho}_{v\vec{G}\vec{G}'}(\vec{q})}{s\omega^+ - \frac{1}{2}\left[\frac{|\vec{q}+\vec{G}|^2}{2} + \frac{|\vec{q}+\vec{G}'|^2}{2}\right] - \frac{f^{\rho j}_{v\vec{G}\vec{G}'}(\vec{q})}{f^{\rho\rho}_{v\vec{G}\vec{G}'}(\vec{q})} \frac{s\omega^+ - \frac{1}{2}\left[\frac{|\vec{q}+\vec{G}|^2}{2} + \frac{|\vec{q}+\vec{G}'|^2}{2}\right] - \frac{f^{\rho j}_{v\vec{G}\vec{G}'}(\vec{q})}{f^{\rho\rho}_{v\vec{G}\vec{G}'}(\vec{q})}}{s\omega^+ - \frac{1}{2}\left[\frac{|\vec{q}+\vec{G}|^2}{2} + \frac{|\vec{q}+\vec{G}'|^2}{2}\right] - \frac{f^{jj}_{v\vec{G}\vec{G}'}(\vec{q})}{f^{\rho j}_{v\vec{G}\vec{G}'}(\vec{q})}}}, \quad (3.26)$$

which will, in general, have more than N_v poles due to the non-linearity of the denominator on the right-hand side.

The above procedure that led to the approximations in Eqs. (3.18) and (3.26) can be continued *ad infinitum* to obtain approximations involving higher order commutators. However, one would hope that already low-order approximations give sufficiently accurate results since higher order approximations become rather complicated. We will show that this is indeed the case. Let us summarize the three approximations we

have obtained so far,

$$\chi^0_{\vec{G}\vec{G}',0}(\vec{q},\omega) = \sum_{s=\pm1}\sum_{v} \frac{f^{\rho\rho}_{v\vec{G}\vec{G}'}(\vec{q})}{s\omega^+ - \frac{1}{2}\left[\frac{|\vec{q}+\vec{G}|^2}{2} + \frac{|\vec{q}+\vec{G}'|^2}{2}\right]} \tag{3.27}$$

$$\chi^0_{\vec{G}\vec{G}',1}(\vec{q},\omega) = \sum_{s=\pm1}\sum_{v} \frac{f^{\rho\rho}_{v\vec{G}\vec{G}'}(\vec{q})}{s\omega^+ - \frac{1}{2}\left[\frac{|\vec{q}+\vec{G}|^2}{2} + \frac{|\vec{q}+\vec{G}'|^2}{2}\right] - \frac{f^{\rho j}_{v\vec{G}\vec{G}'}(\vec{q})}{f^{\rho\rho}_{v\vec{G}\vec{G}'}(\vec{q})}} \tag{3.28}$$

$$\chi^0_{\vec{G}\vec{G}',2}(\vec{q},\omega) = \sum_{s=\pm1}\sum_{v} \frac{f^{\rho\rho}_{v\vec{G}\vec{G}'}(\vec{q})}{s\omega^+ - \frac{1}{2}\left[\frac{|\vec{q}+\vec{G}|^2}{2} + \frac{|\vec{q}+\vec{G}'|^2}{2}\right] - \frac{f^{\rho j}_{v\vec{G}\vec{G}'}(\vec{q})}{f^{\rho\rho}_{v\vec{G}\vec{G}'}(\vec{q})} \frac{s\omega^+ - \frac{1}{2}\left[\frac{|\vec{q}+\vec{G}|^2}{2} + \frac{|\vec{q}+\vec{G}'|^2}{2}\right] - \frac{f^{\rho j}_{v\vec{G}\vec{G}'}(\vec{q})}{f^{\rho\rho}_{v\vec{G}\vec{G}'}(\vec{q})}}{s\omega^+ - \frac{1}{2}\left[\frac{|\vec{q}+\vec{G}|^2}{2} + \frac{|\vec{q}+\vec{G}'|^2}{2}\right] - \frac{f^{jj}_{v\vec{G}\vec{G}'}(\vec{q})}{f^{\rho j}_{v\vec{G}\vec{G}'}(\vec{q})}}}. \tag{3.29}$$

We note that Eqs. (3.28) and (3.29) satisfies several sum rules and exact constraints that are satisfied by the exact $\chi^0(\omega)$ such as the high-frequency limit and the f-sum rule [10].

To obtain GW quasiparticle energies we have to calculate the diagonal matrix elements of the exchange-correlation part of the self-energy. Only the correlation part of the self-energy $\Sigma_{corr}(\omega)$ contains a summation over all the empty states and therefore we will only consider this part of the self-energy in the following. The matrix elements $\Sigma^n_{corr}(\omega) \equiv \langle n|\Sigma_{corr}(\omega)|n\rangle$ are given by

$$\Sigma^n_{corr}(\omega) = \sum_{i=1}^{\infty}\sum_{j\neq0}^{\infty} \frac{|\langle n|V^j|i\rangle|^2}{\omega + \omega_j\,\mathrm{sgn}(\mu-\varepsilon_i) - \varepsilon_i}. \tag{3.30}$$

where $V^j(\vec{r})$ are fluctuation potentials, ω_j are neutral excitation energies of the system (minus a purely imaginary infinitesimal), and μ is the chemical potential. The summation over i in Eqn. (3.30) can be split into a summation over occupied states v with $\varepsilon_v < \mu$ and a summation over empty states c with $\varepsilon_c > \mu$. In the following we will focus on the latter summation since it is the bottleneck in the calculation of Σ^n_{corr} as it sums over the, in principle infinite, empty states of the system. We can rewrite this part as

$$\Sigma^{n,emp}_{corr}(\omega) = \sum_{j\neq0}^{\infty}\sum_{\vec{q},\vec{G},\vec{G}'} V^j_{\vec{G}}(\vec{q}) V^{j*}_{\vec{G}'}(\vec{q}) \sum_{c} \frac{\tilde{\rho}^*_{cn}(\vec{q}+\vec{G})\tilde{\rho}_{cn}(\vec{q}+\vec{G}')}{\omega - \omega_j - \varepsilon_c}, \tag{3.31}$$

in which $V^j_{\vec{G}}(\vec{q})$ is the Fourier transform of $V^j(\vec{r})$. We can eliminate the above summation over empty states in a similar way as we did for the polarizability. The first

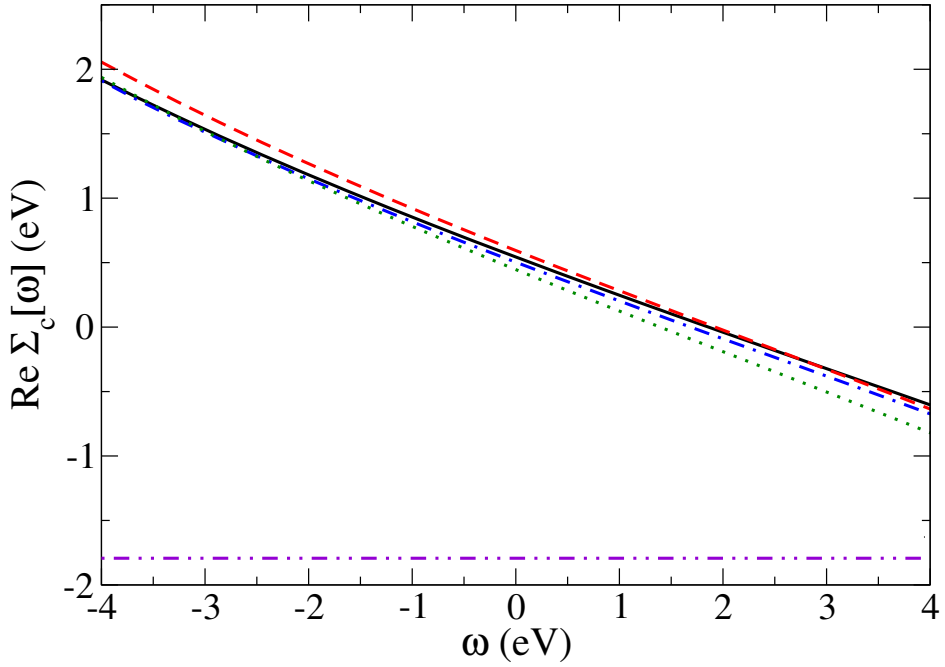

Figure 3.2: The real part of $\Sigma_{corr}(\omega)$ for the highest occupied band at Γ for Si around the LDA orbital energy (set to 0 eV) obtained within G^0W^0. Solid line (black): SOS; dotted line (green): EET using χ_2^0 and $\Sigma_{corr,0}^{emp}$; dashed line (red): EET using χ_2^0 and $\Sigma_{corr,2}^{emp}$; dotted-dashed line (blue): EET using χ_4^0 and $\Sigma_{corr,4}^{emp}$; double-dotted-dashed line (violet): COHSEX.

three approximations are

$$\Sigma_{corr,0}^{n,emp}(\omega)=\sum_{j\neq 0}^{\infty}\sum_{\vec{q},\vec{G},\vec{G}'}V_{\vec{G}}^{j}(\vec{q})V_{\vec{G}'}^{j*}(\vec{q})\frac{f_{n\vec{G}\vec{G}'}^{\rho\rho}(\vec{q})}{\omega-\omega_j-\frac{1}{2}\left[\frac{|\vec{q}+\vec{G}|^2}{2}+\frac{|\vec{q}+\vec{G}'|^2}{2}\right]}, \tag{3.32}$$

$$\Sigma_{corr,1}^{n,emp}(\omega)=\sum_{j\neq 0}^{\infty}\sum_{\vec{q},\vec{G},\vec{G}'}V_{\vec{G}}^{j}(\vec{q})V_{\vec{G}'}^{j*}(\vec{q})\frac{f_{n\vec{G}\vec{G}'}^{\rho\rho}(\vec{q})}{\omega-\omega_j-\frac{1}{2}\left[\frac{|\vec{q}+\vec{G}|^2}{2}+\frac{|\vec{q}+\vec{G}'|^2}{2}\right]-\frac{f_{n\vec{G}\vec{G}'}^{\rho j}}{f_{n\vec{G}\vec{G}'}^{\rho\rho}}}, \tag{3.33}$$

$$\Sigma_{corr,2}^{n,emp}(\omega)=\sum_{j\neq 0}^{\infty}\sum_{\vec{q},\vec{G},\vec{G}'}V_{\vec{G}}^{j}(\vec{q})V_{\vec{G}'}^{j*}(\vec{q})$$
$$\times\frac{f_{n\vec{G}\vec{G}'}^{\rho\rho}(\vec{q})}{\omega-\omega_j-\frac{1}{2}\left[\frac{|\vec{q}+\vec{G}|^2}{2}+\frac{|\vec{q}+\vec{G}'|^2}{2}\right]-\frac{f_{n\vec{G}\vec{G}'}^{\rho j}}{f_{n\vec{G}\vec{G}'}^{\rho\rho}}\left[\frac{\omega_{ng}-Q(\vec{q},\vec{G},\vec{G}')-\frac{f_{n\vec{G}\vec{G}'}^{\rho j}(\vec{q})}{f_{n\vec{G}\vec{G}'}^{\rho\rho}(\vec{q})}\frac{\omega_{ng}-\delta_{ng}(\vec{q},\vec{G},\vec{G}',\omega)}{\omega_{ng}-\tilde{\delta}_{ng}(\vec{q},\vec{G},\vec{G}',\omega)}}{\omega_{ng}-Q(\vec{q},\vec{G},\vec{G}')-\frac{f_{v\vec{G}\vec{G}'}^{jj}(\vec{q})}{f_{n\vec{G}\vec{G}'}^{\rho j}(\vec{q})}\frac{\omega_{ng}-\tilde{\delta}_{ng}(\vec{q},\vec{G},\vec{G}',\omega)}{\omega_{ng}-\tilde{\delta}_{nj}(\vec{q},\vec{G},\vec{G}',\omega)}}\right]} \tag{3.34}$$

We wil now test the quality of the approximations we have obtained for the self-energy and the polarizability. In Fig. 3.2, we report the real part of $\Sigma_{corr}(\omega)$ within G^0W^0 for the highest occupied band of bulk silicon at the Γ point as a function of the frequency around the LDA orbital energy. We compare our EET results using vari-

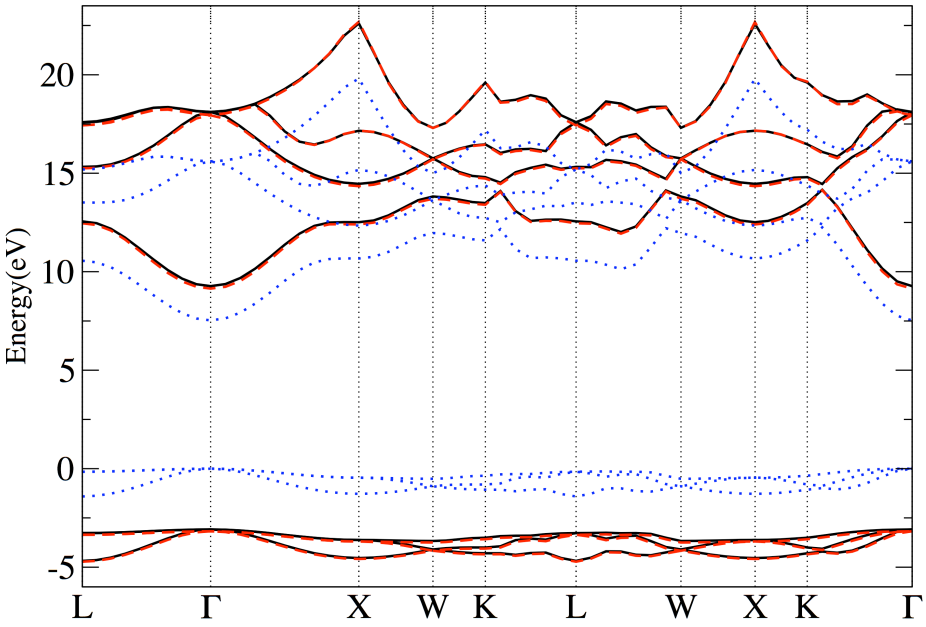

Figure 3.3: Band structure of solid argon. Solid line (black): G^0W^0 (SOS); dashed line (red): G^0W^0 (EET); dotted line (blue): LDA

ous approximations for the polarizability and the self-energy with the converged SOS results obtained with 200 empty bands, and those obtained with the static COHSEX approximation [9], in which empty states are eliminated only in the self-energy but not in the polarizability. Using $\chi_2^0(\omega)$ and $\Sigma_{corr,2}^{emp}(\omega)$ we already obtain results that are in excellent agreement with the SOS result over the whole frequency range of interest, thereby largely improving on the static COHSEX self-energy. With higher-order approximations such $\chi_4^0(\omega)$ and $\Sigma_{corr,4}^{emp}(\omega)$, we can improve the results slightly further (we note that explicit expressions for $\chi_4^0(\omega)$ and $\Sigma_{corr,4}^{emp}(\omega)$ have not been given). However, since, in general, $\chi_2^0(\omega)$ combined with $\Sigma_{corr,2}^{emp}(\omega)$ lead to G^0W^0 results that are in good agreement with the exact SOS results and since the difference with results obtained using higher-order approximations is small, we will use $\chi_2^0(\omega)$ and $\Sigma_{corr,2}^{emp}(\omega)$ in the remainder of this section unless stated otherwise.

We now apply the EET to solid argon because it provides a good test case for two reasons: first, it is a very inhomogeneous systems and therefore very different from the homogeneous systems for which our expressions become exact and, second, the G^0W^0 quasi-particle energies lie far from the LDA energies. In Fig. 3.3, we report the G^0W^0 band structure of solid argon for the three highest occupied bands and four lowest empty bands using the standard SOS approach and the EET. The two band structures are almost indistinguishable. We also report the LDA band structure to show the large difference between the LDA and G^0W^0energies. In Table 3.1, we summarize our EET results for the fundamental gaps of several materials, ranging from silicon to bulk rubrene, an organic molecular crystal with 140 atoms in the unit cell.

	LDA	G^0W^0 (SOS)	G^0W^0 (EET)	COHSEX	Experiment
Silicon (E_g)	0.52	1.20	1.19	1.75	1.17
Silicon ($\Gamma^v - \Gamma^c$)	2.56	3.23	3.22	3.76	3.40
Solid Argon (E_g)	7.53	12.4	12.3	14.2	
Argon atom (HOMO-LUMO)	9.81	14.6	14.5	15.8	-
SnO_2	0.91	2.89	2.94	4.61	3.6
ZnO	0.82	2.56	2.39	-	3.4
Rubrene (crystal)	1.13	2.5	2.7	-	-

Table 3.1: Fundamental gaps E_g of silicon, solid argon, SnO_2, ZnO, and crystalline rubrene, the direct band gap at Γ of silicon and the HOMO-LUMO gap of atomic argon. All gaps are in eV.

We also report the direct band gap at Γ of silicon and the highest occupied molecular orbital (HOMO)-lowest unoccupied molecular orbital (LUMO) gap of atomic argon. We obtain a large improvement with respect to the COHSEX results which largely overestimate the G^0W^0 band gaps and a very good agreement with the SOS approach.

As an example, let us have a closer look at SnO_2. The SOS calculations for SnO_2 required 1000 and 1600 bands, respectively, to arrive at a convergence of 10 meV for the gaps, while the EET calculations just required 34 occupied bands. The SnO_2 band gap within G^0W^0 of 2.9 eV is not in good agreement with the experimental band gap of 3.6 eV. This is due to the fact that the LDA energies and wave functions do not provide a good starting point for the G^0W^0 calculation. However, within the GW method, we can recalculate the screening and self-energy using updated energies and wave functions by including some form of self-consistency. Using the SOS approach, even the simplest GW method involving self-consistency, the self-consistent COHSEX+G^0W^0 approach [11] is computationally quite demanding because $\chi^0(\omega)$ has to be recalculated. This means that the energies and wave functions have to be updated during self-consistency. This bottleneck can now be overcome by applying the EET to the calculation of both the static polarizability in the self-consistent COHSEX approach and the G^0W^0 self-energy. We can thus include self-consistency effects using summations over occupied states only. Using the EET, we are now able to determine the GW band gap of SnO_2 to be 3.8 eV which is in good agreement with experiment. This result is summarized in Table 3.2.

	LDA	GW+EET	Experiment
SnO_2 (E_g)	0.91	3.8	3.6

Table 3.2: Fundamental gap E_g in eV of SnO_2 obtained with self-consistent COHSEX + G^0W^0 (GW) using the EET.

Up to this point we have used the EET to obtain approximations to the GW self-energy and the independent-particle polarizability which do not contain summations over empty states. Although we have shown that simple approximations, such as $\chi_2^0(\omega)$ and $\Sigma_{corr,2}^{emp}(\omega)$, are accurate and numerically efficient, one might wish to converge to the numerically exact GW result. Such numerically exact results can be obtained efficiently and in a systematic way by combining the EET and the SOS approach. Let us illustrate how we achieve this goal for the polarizability. We first split the summation over the empty states in Eqn. (3.1) into two parts according to

$$\chi^0_{\vec{G}\vec{G}'}(\vec{q},\omega) = \sum_{s=\pm 1}\sum_{v}\left[\sum_{c=N_v+1}^{M}\frac{\tilde{\rho}^*_{cv}(\vec{q}+\vec{G})\tilde{\rho}_{cv}(\vec{q}+\vec{G}')}{s\omega^+ - (\epsilon_c-\epsilon_v)} + \sum_{c=M+1}^{\infty}\frac{\tilde{\rho}^*_{cv}(\vec{q}+\vec{G})\tilde{\rho}_{cv}(\vec{q}+\vec{G}')}{s\omega^+ - (\delta_{v\vec{G}\vec{G}'}(\vec{q},s\omega^+)-\epsilon_v)}\right], \tag{3.35}$$

where we used the EET only in the second term on the right-hand side which contains a summation over all the empty states starting from $M+1$. If we choose $M = N_v$ we retrieve Eqn. (3.2). However, if we choose $M > N_v$ the part that needs to be approximated with the EET becomes smaller as $M - N_v$ increases. In this way we have obtained an efficient way to converge $\chi_0(\omega)$ with respect to the number of empty states.

Since we will now converge the quasi-particle energies and band gaps with respect to the number of empty states, we can combine the very simple approximation given in Eq. (3.27) with the SOS approach according to

$$\begin{aligned}\chi^0_{\vec{G}\vec{G}'}(\vec{q},\omega) = \sum_{s=\pm 1}\sum_{v}\Bigg[&\sum_{c=N_v+1}^{M}\frac{\tilde{\rho}^*_{cv}(\vec{q}+\vec{G})\tilde{\rho}_{cv}(\vec{q}+\vec{G}')}{s\omega^+ - (\epsilon_c-\epsilon_v)} \\ &+ \sum_{c=M+1}^{\infty}\frac{\tilde{\rho}^*_{cv}(\vec{q}+\vec{G})\tilde{\rho}_{cv}(\vec{q}+\vec{G}')}{s\omega^+ - \frac{1}{2}\left[\frac{|\vec{q}+\vec{G}|}{2}+\frac{|\vec{q}+\vec{G}'|}{2}\right]-\epsilon_v)}\Bigg].\end{aligned} \tag{3.36}$$

A similar approach can be used for the self-energy. Here we will use $\Sigma_{corr,0}^{emp}(\omega)$ given in Eq. (3.32). This above procedure can be seen as a generalization of the one proposed by Bruneval and Gonze [12], the difference being that our approach is parameter free. With this SOS+EET approach we can obtain converged quasi-particle energies using only very few empty states.

To illustrate the SOS+EET approach we report in Fig. 3.4 the convergence behavior of the valence-band maximum (VBM), conduction band minimum (CBM) and band gap of SnO_2 with the number of empty states using the standard SOS approach and the SOS+EET approach. We see that using the SOS+EET approach numerical convergence of 10 meV is reached with slightly more than 100 empty bands. This is true, not only for the band gap, but also for the absolute quasi-particle energies at the VBM and CBM which are much harder to converge since there is no error cancelation. By contrast, the SOS approach has not reached convergence for any of these quantities with as much as 800 empty bands

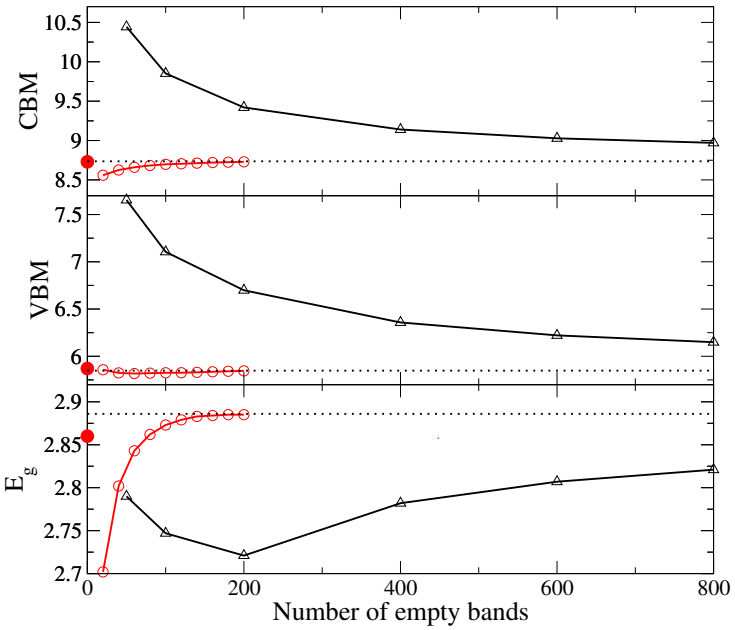

Figure 3.4: Convergence behavior of the VBM, CBM, and fundamental gap (E_g) of SnO_2 in eV with the number of empty states in both the screening and self-energy calculcations. Black triangles: SOS approach; red open circles: SOS+EET approach using $\delta'^{(0)}$ and $\delta^{(0)}$; red filled circles: EET using $\chi_2^0(\omega)$ and $\Sigma_{corr,2}^{emp}(\omega)$ without empty states. The dotted line is a guide to the eye.

We can now compare the converged SOS+EET results with those obtained with our approximate EET scheme using no empty states. This comparison is reported in Table 3.3. We conclude that the values we obtained with our EET using $\chi_2^0(\omega)$ and $\Sigma_{corr,2}^{emp}(\omega)$ are in excellent agreement with the numerically exact values.

There has been much debate on the numerically exact value of the G^0W^0 band gap of ZnO, and in particular, the number of empty bands required to reach convergence [13–16]. Therefore we applied our SOS+EET approach to obtain a G^0W^0 band gap that is converged with respect to the number of empty states. In Fig. 3.5 we report the convergence behavior of the VBM, CBM and band gap of ZnO with the number of empty states using the standard SOS approach and the SOS+EET approach. We see that the band gap using the SOS+EET approach does not converge as quickly as

	LDA	G^0W^0 (EET)	G^0W^0 (SOS+EET)
CBM	8.20	8.73	8.74
VBM	7.26	5.87	5.85
E_g	0.94	2.86	2.89

Table 3.3: Calculated energies for the VBM, CBM, and fundamental gap (E_g) in eV of SnO_2. The last column contains numerically converged G^0W^0 quasiparticle energies.

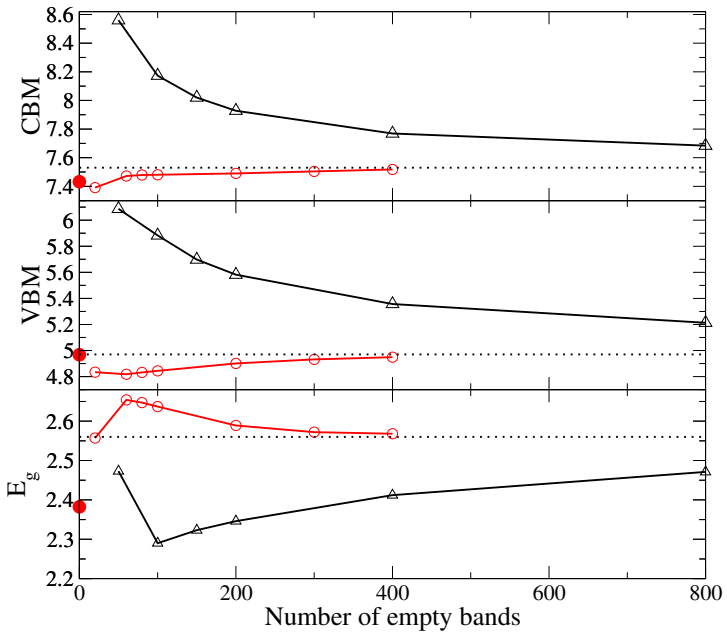

Figure 3.5: Convergence behavior of the VBM, CBM, and fundamental gap (E_g) in eV of ZnO with the number of empty states in both the screening and self-energy calculcations. Black triangles: SOS approach; red open circles: SOS+EET approach using $\delta'^{(0)}$ and $\delta^{(0)}$; red filled circles: EET using $\chi_2^0(\omega)$ and $\Sigma_{corr,2}^{emp}(\omega)$ without empty states. The dotted line is a guide to the eye.

was the case for SnO_2 but convergence is still reached much faster than with the SOS approach alone. We conclude that the converged G^0W^0 band gap of ZnO is 2.56 eV. The results for the VBM, CBM and band gap of ZnO are summarized in Table 3.4. We refer the reader to the work of Stankovski *et al.* [16] for more details on the issue of the G^0W^0 band gap of ZnO.

In summary, we have given an overview of the effective-energy technique, a simple method to evaluate spectral representations in an accurate and efficient manner without summing over empty states as is done in the standard sum-over-states approach. In particular, we showed how the effective-energy technique can be applied to reformulate the expressions for the GW self-energy and the independent-particle polarizability in terms of occupied states only by introducing a single effective energy

	LDA	G^0W^0 (EET)	G^0W^0 (SOS+EET)
VBM	6.38	5.04	4.97
CBM	7.19	7.43	7.53
E_g	0.82	2.39	2.56

Table 3.4: Calculated energies for the VBM, CBM, and fundamental gap (E_g) in eV of ZnO. The last column contains numerically converged G^0W^0 quasiparticle energies.

which takes into account all the empty states. We also showed how one can obtain in an efficient way numerically exact G^0W^0 quasi-particle energies by combining the effective-energy technique with a sum-over-states approach.

3.2 Fully parameter-free calculation of the optical spectra for insulators, semiconductors and metals from a simple polarization functional

In the previous section we showed how one can obtain in a numerically efficient way quasi-particle energies using the effective-energy technique. The quasi-particle energies contain important information about the system since they are the removal and addition energies but, they also provide an accurate starting point for the calculation of response properties, since they are used to build the response functions. In this section we will show how starting from these quasi-particle energies one can obtain accurate optical absorption spectra within time-dependent current-density functional theory using a simple polarization functional.

corresponding publication

- *Fully parameter-free calculation of optical spectra for insulators, semiconductors and metals from a simple polarization functional*
  J. A. Berger
  Phys. Rev. Lett. **115**, 137402 (2015)

The state-of-the-art approach to calculate absorption spectra of solids is the Bethe-Salpeter equation (BSE) [17–20]. It is related to the particle-hole part of the two-particle Green's function and therefore explicitly takes into account the interaction between the excited electron and the hole it leaves behind in an absorption process. From the two-particle nature of absorption processes it is clear that to obtain a similar quality of spectra as the BSE within time-dependent density-functional theory (TDDFT) [3] or time-dependent current-density-functional theory (TDCDFT) [5–7] is a formidable challenge since two-particle processes should be described through an effective potential of the noninteracting Kohn-Sham system. Nevertheless, the search for such an effective potential is worthwhile since the numerical advantage to be gained is significant. A straightforward implementation of the BSE scales as N^6 where N is the number of atoms or electrons in the unit cell while a straightforward implementation of the TD(C)DFT equations scales as N^4 or N^3.

Considering the above it is no surprise that standard approximations, *i.e.*, the random-phase approximation (RPA) and the adiabatic local-density approximation (ALDA) [21] are incapable of accurately describing optical spectra. Their failures are numerous: 1) they underestimate the absorption onset; 2) they cannot describe Drude tails in the spectra of metals; 3) they underestimate the intensity of continuum excitons; 4) they cannot describe bound excitons. While the first problem has not yet found a solution within TD(C)DFT it can be circumvented by replacing the Kohn-Sham eigenvalues by *GW* quasiparticle energies [8, 9], which can be efficiently

calculated with the effective-energy technique. As we will show the other three problems we can solve within TDCDFT.

The first approximations specifically designed for the calculation of optical spectra in TD(C)DFT were mainly interested in the correct description of continuum excitons. This can be achieved by applying a long-range exchange-correlation (xc) kernel [22–24]. However, a material-dependent parameter is needed to get results that are quantitatively correct. Instead, the nanoquanta kernel [25–29] is parameter free and can correctly describe continuum as well as bound excitons. However, the nanoquanta kernel is derived from the BSE and, therefore, it is basically as expensive to evaluate as the BSE. Instead, the Vignale-Kohn current functional [30] is simple to evaluate [31] and describes well the optical spectra of metals [32]. However, it does not describe correctly excitons in semiconductors and insulators [33].

Recently there is a renewed interest to go beyond these approximations and try to obtain BSE-like spectra with a parameter-free and numerically efficient density-functional approach. This is mainly thanks to the bootstrap method proposed in Ref. [34] in which optical spectra of good quality were reported. Although some problems were found with the bootstrap method [35–38] it gave a strong impetus to the search for new approximations [35, 39–43].

With respect to other approaches the advantages of our method [43] can be summarized as follows: 1) Our xc kernel is parameter free, not even a material-dependent broadening parameter is needed; 2) Our xc kernel is dynamical and can therefore take into account memory effects and describe Drude tails and the finite width of bound excitons; 3) The cost of a calculation is equal to that of a calculation within the RPA; 4) Our approach avoids the explicit calculation of Kohn-Sham response functions leading to numerical efficiency.

Absorption spectra are related to the imaginary part of the macroscopic dielectric tensor $\overleftrightarrow{\epsilon}_M$. Let us briefly explain how it can be obtained from knowledge of the induced current density of the bulk only. The macroscopic polarization can be defined as a bulk property according to

$$\vec{P}_{mac}(\omega) = \frac{-i}{\omega V} \int_V d\vec{r} \delta\vec{j}(\vec{r}, \omega). \tag{3.37}$$

where $\delta\vec{j}(\vec{r}, \omega)$ is the induced current density in the bulk and V is the volume of the unit cell. The macroscopic polarization is induced by a macroscopic electric field $\vec{E}_{mac}(\omega)$ which comprises both the externally applied field and the macroscopic induced electric field [44]. The constant of proportionality is the electric susceptibility tensor $\overleftrightarrow{\chi}_e(\omega)$ which is defined as

$$\vec{P}_{mac}(\omega) = \overleftrightarrow{\chi}_e(\omega) \cdot \vec{E}_{mac}(\omega). \tag{3.38}$$

The macroscopic dielectric tensor $\overleftrightarrow{\epsilon}_M(\omega)$ can be obtained from the electric susceptibility according to

$$\overleftrightarrow{\epsilon}_M(\omega) = 1 + 4\pi \overleftrightarrow{\chi}_e(\omega). \tag{3.39}$$

Therefore, for a given $E_{mac}(\omega)$, from the knowledge of the induced bulk current only, one can calculate $\overleftrightarrow{\epsilon}_M(\omega)$ using Eqs. (3.37)-(3.39). This procedure is general, *i.e.*, it can be combined with any theory that allows for the calculation of the induced bulk current density. A very efficient approach to calculate the current density is time-dependent current-density functional theory (TDCDFT) [5–7]. In this theory the problem of finding the true bulk current density of the interacting system is mapped onto a noninteracting system governed by a set of effective Kohn-Sham potentials $\{v_{KS}, \vec{A}_{KS}\}$ that reproduce the bulk current density of the interacting system. Here v_{KS} and $\vec{A}_{KS}$ are the Kohn-Sham scalar and vector potential, respectively. They are defined up to a gauge choice.

Within the linear-response regime the current density is given by

$$\delta\vec{j}(\vec{r},\omega) = \int d\vec{r}' \overleftrightarrow{\chi}^{KS,\vec{j}\vec{j}}(\vec{r},\vec{r}',\omega)\cdot[\vec{A}_{mac}(\omega)+\vec{A}^{xc}(\vec{r}',\omega)]+\int d\vec{r}' \vec{\chi}^{KS,\vec{j}\rho}(\vec{r},\vec{r}',\omega)\delta v_{mic}^{Hxc}(\vec{r}',\omega). \tag{3.40}$$

Here we used the microscopic Coulomb gauge in which the microscopic potential $\delta v_{mic}^{Hxc}(\vec{r},\omega)$ is lattice periodic and contains the periodic part of the Hartree and longitudinal xc contributions [44]. All remaining xc contributions are included in the vector potential $\vec{A}^{xc}(\vec{r},\omega)$. In this work we focus on finding an accurate approximation for $\vec{A}^{xc}_{mac}(\omega)$, the macroscopic part of $\vec{A}^{xc}(\vec{r},\omega)$. Therefore, in the following we will neglect microscopic transverse xc contributions to $\vec{A}^{xc}(\vec{r},\omega)$.

Let us now define the Kohn-Sham electric field according to

$$\vec{E}^{KS}_{mac}(\omega) = \vec{E}_{mac}(\omega) + \vec{E}^{xc}_{mac}(\omega). \tag{3.41}$$

We note that the electric field and the vector potential are interchangeable since they are related by the simple expression: $\vec{E}(\omega) = i\omega\vec{A}(\omega)$. The substitution of Eq. (3.40) into Eq. (3.37) shows that $\vec{P}_{mac}(\omega)$ is linear in $\vec{E}^{KS}_{mac}(\omega)$:

$$\begin{aligned}\vec{P}_{mac}(\omega) = \frac{-1}{\omega^2 V}\left[\int_V d\vec{r}\int d\vec{r}' \overleftrightarrow{\chi}^{KS,\vec{j}\vec{j}}(\vec{r},\vec{r}',\omega)\right]\cdot\vec{E}^{KS}_{mac}(\omega) \\ + \frac{-i}{\omega V}\int_V d\vec{r}\int d\vec{r}' \vec{\chi}^{KS,\vec{j}\rho}(\vec{r},\vec{r}',\omega)\delta v_{mic}^{Hxc}(\vec{r}',\omega).\end{aligned} \tag{3.42}$$

It is useful to define the Kohn-Sham susceptibility $\overleftrightarrow{\chi}^{KS}_e$ according to [22]

$$\vec{P}_{mac}(\omega) = \overleftrightarrow{\chi}^{KS}_e(\omega)\cdot\vec{E}^{KS}_{mac}(\omega). \tag{3.43}$$

A comparison of Eqs. (3.38) and (3.43) reveals that

$$\left([\overleftrightarrow{\chi}^{KS}_e]^{-1}(\omega) - [\overleftrightarrow{\chi}_e]^{-1}(\omega)\right)\cdot\vec{P}_{mac}(\omega) = \vec{E}^{xc}_{mac}(\omega). \tag{3.44}$$

where we used Eqn. (3.41). When using approximations such as RPA and ALDA, which have no macroscopic component, one implicitly sets $\vec{E}^{xc}_{mac}(\omega) = 0$ and, as a consequence, Eqn. (3.44) tells us that the true susceptibility is approximated by that of the

Kohn-Sham system, *i.e.*, $\overleftrightarrow{\chi}_e(\omega) = \overleftrightarrow{\chi}_e^{KS}(\omega)$. Here we go beyond this simple approximation. We note that, nevertheless, even in the RPA and ALDA, the contributions of $\delta v_{mic}^{Hxc}(\vec{r},\omega)$ to $\overleftrightarrow{\chi}_e$ are fully taken into account as can be seen from Eqn. (3.42). Since $\delta v_{mic}^{Hxc}(\vec{r},\omega)$ is itself a functional of $\delta\vec{j}(\vec{r},\omega)$ this is done within a self-consistent field (SCF) calculation. We will now show that macroscopic xc effects can be accounted for through $\vec{E}_{mac}^{xc}(\omega)$ post-SCF.

The macroscopic xc electric field is related to the induced current through the TDCDFT tensor xc kernel $\overleftrightarrow{f}_{xc}(\vec{r},\vec{r}',\omega)$ according to

$$\vec{E}_{mac}^{xc}(\omega) = \frac{i\omega}{V}\int_V d\vec{r}\int d\vec{r}'\overleftrightarrow{f}_{xc}(\vec{r},\vec{r}',\omega)\cdot\delta\vec{j}(\vec{r}',\omega). \tag{3.45}$$

By neglecting microscopic current components in Eq. (3.45), *i.e.*, substituting $\delta\vec{j}(\vec{r},\omega)$ by its unit-cell average, we obtain a polarization functional for $\vec{E}_{mac}^{xc}(\omega)$:

$$\vec{E}_{mac}^{xc}(\omega) = \overleftrightarrow{\alpha}(\omega)\cdot\vec{P}_{mac}(\omega), \tag{3.46}$$

where we used Eq. (3.37) and in which we defined

$$\overleftrightarrow{\alpha}(\omega) = -\frac{\omega^2}{V}\int_V d\vec{r}\int d\vec{r}'\overleftrightarrow{f}_{xc}(\vec{r},\vec{r}',\omega). \tag{3.47}$$

The substitution of Eq. (3.46) into Eq. (3.44) leads to

$$[\overleftrightarrow{\chi}_e]^{-1}(\omega) = [\overleftrightarrow{\chi}_e^{KS}]^{-1}(\omega) - \overleftrightarrow{\alpha}(\omega). \tag{3.48}$$

Therefore, for a given $\overleftrightarrow{\alpha}(\omega)$, we can readily calculate $\overleftrightarrow{\chi}_e(\omega)$ from $\overleftrightarrow{\chi}_e^{KS}(\omega)$. Here we will use the RPA ($\delta v_{mic}^{Hxc} = \delta v_{mic}^{H}$) to calculate $\overleftrightarrow{\chi}_e^{KS}(\omega)$, *i.e.*, $\overleftrightarrow{\chi}_e^{KS} = \overleftrightarrow{\chi}_e^{RPA}$. Since continuum excitons are underestimated and bound excitons and Drude tails are absent in RPA optical spectra, we will include these effects through $\alpha(\omega)$. Whether the macroscopic dielectric function corresponding to $\overleftrightarrow{\chi}_e$ will be an improvement to that corresponding to $\overleftrightarrow{\chi}_e^{RPA}$ depends of course on the choice for $\alpha(\omega)$. We will now briefly describe how an approximation can be obtained. For simplicity, we assume that $\overleftrightarrow{\chi}_e(\omega)$, $\overleftrightarrow{\chi}_e^{RPA}(\omega)$ and $\overleftrightarrow{\alpha}(\omega)$ are isotropic, *i.e.*, $\alpha_{ij}(\omega) = \alpha(\omega)\delta_{ij}$, etc.. Let us first restrict ourselves to a static α. In this case a bound exciton can only obtained if for the frequency at which the bound exciton occurs, ω_{be}, with ω_{be} smaller than the band gap, we have [25]

$$\mathrm{Re}[\alpha(\omega_{be})] = \frac{1}{\chi_e^{RPA}(\omega_{be})}, \tag{3.49}$$

and $\mathrm{Im}[\alpha(\omega_{be})]$ vanishes or is small.

Although the constaint given in Eq. (3.49) is important, it does not tell us how to apply it in practice because ω_{be} is unknown. In fact, we would like to deduce ω_{be} from the calculation. Bound excitons are visible in the absorption spectra only of systems in which screening effects are small, *i.e.*, systems with a small dielectric constant,

$1 < \epsilon_M(\omega = 0) \lesssim 2$, *e.g.*, LiF and solid argon, Since the RPA dielectric constant is, in general, close to the exact one, we can also write $1 < \epsilon_M^{RPA}(\omega = 0) \lesssim 2$. For these systems and for frequencies below the quasi-particle gap, $\chi_e^{RPA}(\omega)$ is a function that is purely real and increases slowly and monotonically. Since by definition ω_{be} is smaller than the band gap, we therefore have that $1 < \frac{\chi_e^{RPA}(\omega_{be})}{\chi_e^{RPA}(\omega=0)} \lesssim 2$. The above considerations suggest the following approximation

$$\epsilon_M^{RPA}(\omega = 0) \approx \frac{\chi_e^{RPA}(\omega_{be})}{\chi_e^{RPA}(\omega = 0)}. \tag{3.50}$$

Substitution of this approximation into Eq. (3.49) then leads to

$$\alpha \equiv \mathrm{Re}[\alpha(\omega_{be})] = \frac{1}{\chi_e^{RPA}(0)\epsilon_M^{RPA}(0)}. \tag{3.51}$$

which can now be calculated from the knowledge of $\chi_e^{RPA}(0)$ alone. The derivation of Eq. (3.51) can be made more rigorous by studying a model insulator for which the optical spectrum is dominated by a bound exciton and perform a Taylor expansion of $\chi_e^{RPA}(\omega)$ around $\omega = 0$ for this simple model and evaluate the expansion at $\omega = \omega_{be}$ [43].

We note that an expression similar to Eq. (3.51) was found in Ref. [35] within the context of TDDFT. What is particularly interesting is that, contrary to the derivation given above, which assumes a small dielectric constant, the derivation given in Ref. [35] assumes a large dielectric constant. The fact that, despite this important difference, the final results are similar is encouraging and hints at a wide applicability of the α given in Eq. (3.51). Another argument points to the same conclusion. Numerically it has been shown that an α that is proportional to $[\epsilon_M^{RPA}(0)]^{-1}$ can lead to good optical spectra for semiconductors since $\epsilon_M^{RPA}(0)$ is a measure of the screening of the interaction between the electron and the hole it leaves behind in an absorption process [24, 45] .

The main problem with the kernel given in Eq. (3.51) is that it is static. As a consequence it cannot take into account Drude tails nor the finite width of bound excitons. A functional that could account for these features is the frequency-dependent Vignale-Kohn functional [30]. This functional is exact for a slightly inhomogeneous electron gas [30] and it can describe Drude tails in the optical spectra of metals [32]. However, as mentioned before, this functional is not able to describe excitons. From the above discussion we conclude that the kernel in Eq. (3.51) and the VK functional are, to a large extent, complementary. While Eq. (3.51) accounts for continuum excitons and the position of bound excitons, the VK functional accounts for Drude tails and the finite width of the bound excitons. Moreover, the static kernel in Eq. (3.51) tends to zero for metals since screening is complete and as a consequence $[\epsilon_M^{RPA}(\omega = 0)]^{-1} \to 0$. It therefore seems natural to combine the two functionals.

Since in this work we focus on the macroscopic part of the xc vector potential we will consider only the macroscopic average of the VK xc vector potential. Moreover,

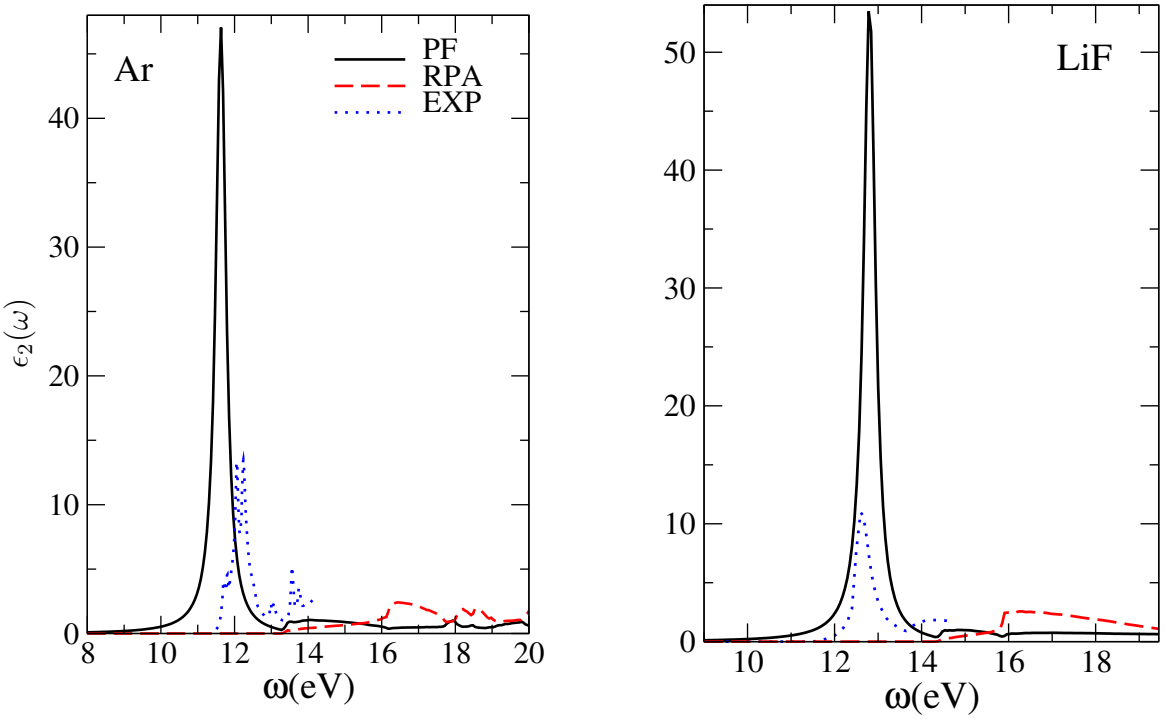

Figure 3.6: The optical absorption spectra of solid Argon and LiF. Solid line (black): polarization functional (PF); Dashed line (red): RPA; Dotted line (blue): experiment from Ref. [46] (Ar) and Ref. [47] (LiF).

to arrive at a polarization functional we replace the current density by its unit-cell average. The resulting kernel is given by [22]

$$\overleftrightarrow{Y}_{VK}(\omega) = \frac{1}{V}\int_V d\vec{r}\left(\frac{\nabla\rho_0(\vec{r})\cdot\nabla\rho_0(\vec{r})}{\rho_0^2(\vec{r})} f_{xcT}(\bar{\rho},\omega)\overleftrightarrow{\mathrm{I}} + \frac{\nabla\rho_0(\vec{r})\otimes\nabla\rho_0(\vec{r})}{\rho_0^2(\vec{r})}\left[f_{xcL}(\bar{\rho},\omega) - f_{xcT}(\bar{\rho},\omega) - \frac{d^2 e_{xc}}{d\bar{\rho}^2}\right]\right). \tag{3.52}$$

Here $f_{xcL(T)}(\omega)$ is the longitudinal (transverse) xc kernel of the homogeneous electron gas, e_{xc} is the xc energy per volume of the homogeneous electron gas, $\rho_0(\vec{r})$ is the ground-state density and $\bar{\rho}$ is its average in a unit cell.

We finally obtain the following approximation for $\overleftrightarrow{\alpha}(\omega)$,

$$\overleftrightarrow{\alpha}(\omega) = [\overleftrightarrow{\epsilon}_M^{RPA}(0)]^{-1}[\overleftrightarrow{\chi}_e^{RPA}(0)]^{-1} + \overleftrightarrow{Y}_{VK}(\omega) \tag{3.53}$$

where we generalized Eq. (3.51) to a tensor form. Since $[\overleftrightarrow{\epsilon}_M^{RPA}(0)]^{-1}$ and $[\overleftrightarrow{\chi}_e^{RPA}(0)]^{-1}$ commute, the order of the multiplication is irrelevant.

In Fig. 3.6 we show the optical absorption spectra of solid argon and LiF obtained with our polarization functional and compare it to the RPA spectra and to experimental results. Solid argon and LiF are typical materials that exhibit strongly bound

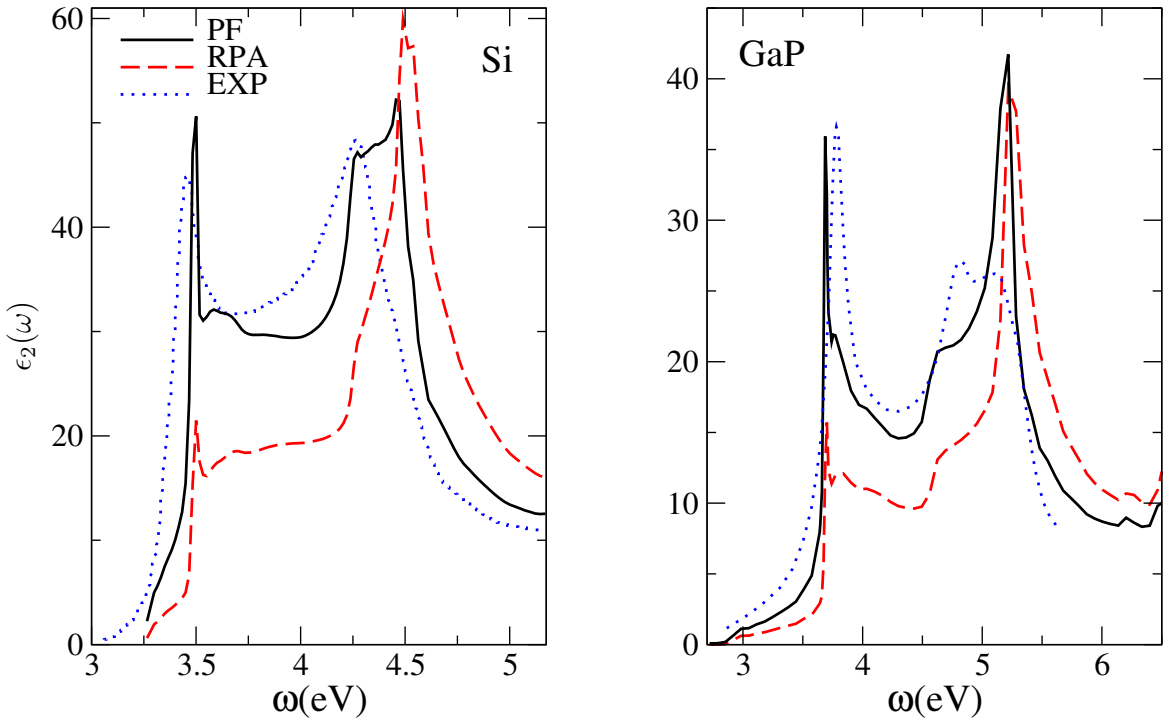

Figure 3.7: The optical absorption spectra of bulk silicon and GaP. Solid line (black): polarization functional (PF); Dashed line (red): RPA; Dotted line (blue): experiment from Ref. [48] (Si) and Ref. [49] (GaP).

excitons. We see that these excitons which appear in the experimental spectra around 12 eV (Ar) and 12.5 eV (LiF) are completely absent in the RPA spectra. Our polarization functional describes these bound excitons and also accurately reproduces their position. However, the magnitude of the peaks is overestimated with respect to experiment. Also other density-functional approaches tend to overestimate these peaks [34, 40]. Finally, we verify *a posteriori* whether the approximation in Eq. (3.50) for systems with a small dielectric constants was justified. For LiF the left-hand side (LHS) and right-hand side (RHS) of Eq. (3.50) are, respectively, 1.77 and 1.78. For solid Ar the LHS and RHS of Eq. (3.50) are, respectively, 1.64 and 1.60. We therefore conclude that Eq. (3.50) was justified.

In Fig. 3.7 we report the optical absorption spectra of bulk silicon and bulk GaP obtained with our polarization functional and compare it to the RPA spectra and to experimental results. Silicon and GaP are typical examples of materials for which the RPA strongly underestimates the first peak which appears in the experimental spectra around 3.4 eV (Si) and 3.8 eV (GaP). Our polarization functional solves this problem by including the necessary excitonic effects and the first peak compares well with experiment both in position and magnitude. Overall, the spectra are very close to experiment with the exception of the peak around 5.2 eV in the spectrum of GaP which is overestimated.

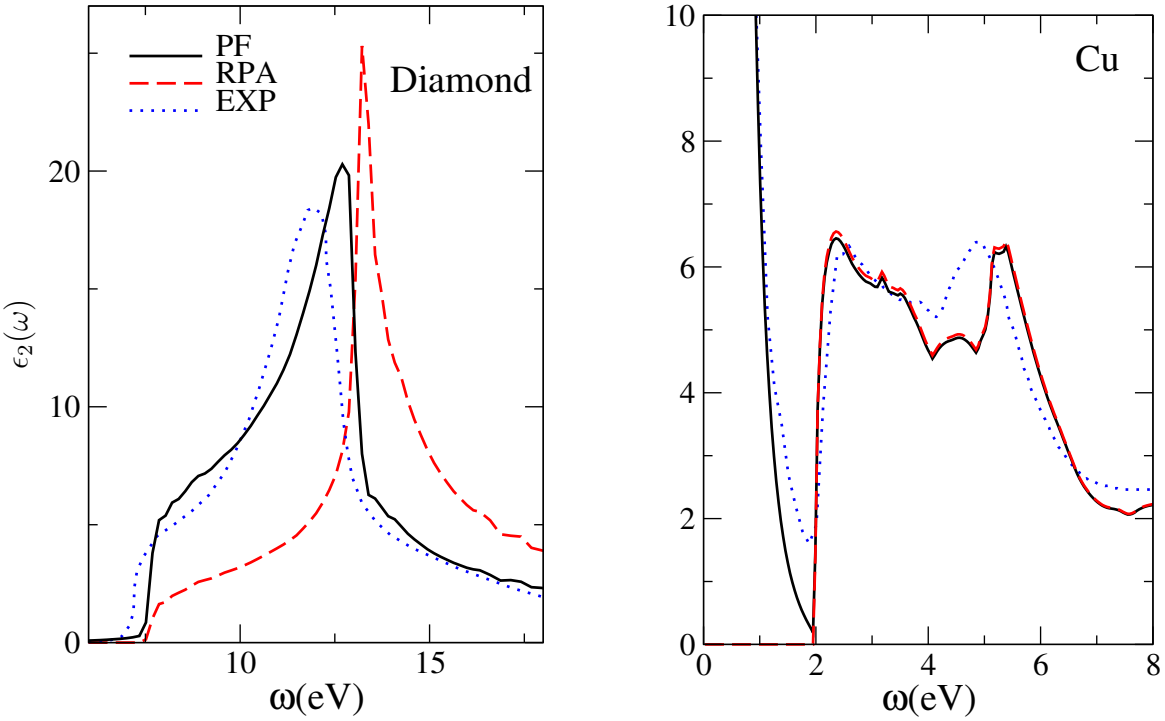

Figure 3.8: The optical absorption spectra of diamond and copper. Solid line (black): polarization functional (PF); Dashed line (red): RPA; Dotted line (blue): experiment from Ref. [50] (Diamond) and Refs. [51] and [52] (Cu).

In Fig. 3.8 we report the optical absorption spectra of diamond and copper obtained with the polarization functional and compare it to the RPA spectra and to experimental results. Diamond is another typical test case since the RPA spectrum is quite different from the experimental spectrum. Due to the absence of excitonic effects the RPA spectrum has too much weight at high energy. With our polarization functional the spectral weight is shifted to lower energy and we obtain a very good agreement with experiment. While the RPA spectrum of copper accurately reproduces the part of the spectrum which is due to interband transitions, the Drude tail at low energy, which is due to intraband transitions, is completely absent. Our polarization functional accurately describes the Drude tail while maintaining the good agreement for the interband part.

In conclusion, we presented a fully parameter-free density-functional approach that gives accurate optical spectra for insulators, semiconductors and metals alike. Our approach is therefore truly predictive.

3.3 Gauge-Invariant Calculation of Static and Dynamical Magnetic Properties from the Current Density

In the previous section we limited ourselves to perturbations due to electric fields and we discussed a purely electric response property, namely the optical absorption spectra of solids. We will now turn our attention towards response properties that also have a magnetic component. In this section we will focus on molecules and show that already for these finite systems interesting problems occur and, in particular, the problem of obtaining gauge-invariant results. We leave the discussion of the challenges related to the description of the magnetic response of extended systems to the next chapter.

corresponding publications

- *Gauge-Invariant Calculation of Static and Dynamical Magnetic Properties from the Current Density*
  N. Raimbault, P. L. de Boeij, P. Romaniello, and J. A. Berger
  Phys. Rev. Lett. **114**, 066404 (2015)

- *Gauge-invariant Formulation of Circular Dichroism*
  N. Raimbault, P. L. de Boeij, P. Romaniello, and J. A. Berger
  J. Chem. Theory Comput. **12**, 3278 (2016)

The definitions of (electro-)magnetic properties, such as the magnetizability and the optical rotation tensor, are usually obtained from multipole theory. A fundamental characteristic of these definitions is that they depend on the particular choice of the point of reference in the multipolar expansion. This point of reference can be easily confused with the origin of the system of coordinates leading to results that depend on the choice of this origin. Although the above problem does not affect static properties, both static and dynamic properties suffer from an artificial dependence on the point of reference in the vector potential, which represents the external electromagnetic fields, when a finite basis set is used. Moreover, this artificial dependence corresponds to a very slow convergence with the size of the basis. As we will show this problem is related to the fact that the paramagnetic and diamagnetic contributions to magnetic properties are not treated on an equal footing.

To illustrate this problem we will study the magnetizability and the optical rotation tensor. The magnetizability tensor $\overleftrightarrow{\xi}$ is defined as the constant of proportionality of the induced magnetic dipole moment $\delta\vec{m}(\omega)$ and an externally applied uniform magnetic field $\vec{B}(\omega)$:

$$\delta m_i(\omega) = \sum_j \xi_{ij}(\omega) B_j(\omega). \tag{3.54}$$

The optical rotation tensor can be defined in two ways, $\overleftrightarrow{G}$ is defined as the constant of proportionality of the induced electric dipole moment $\delta\vec{p}(\omega)$ and an externally applied uniform magnetic field $\vec{B}(\omega)$ while $\overleftrightarrow{\tilde{G}}$ is defined as the constant of proportionality of the induced magnetic dipole moment $\delta\vec{p}(\omega)$ and an externally applied uniform electric field $\vec{E}(\omega)$:

$$\delta p_i(\omega) = \sum_j G_{ij}(\omega) B_j(\omega), \tag{3.55}$$

$$\delta m_i(\omega) = \sum_j \tilde{G}_{ij}(\omega) E_j(\omega). \tag{3.56}$$

Performing a multipole expansion around a fixed reference point in the molecular frame $\vec{r}_C$, leads to the following definitions for $\delta\vec{p}(\omega)$ and $\delta\vec{m}(\omega)$,

$$\delta\vec{p}(\omega) = \int d\vec{r}(\vec{r} - \vec{r}_C)\delta\rho(\vec{r},\omega) = \frac{i}{\omega}\int d\vec{r}\delta\vec{j}(\vec{r},\omega) \tag{3.57}$$

$$\delta\vec{m}(\vec{r}_C,\omega) = \frac{1}{2}\int d\vec{r}(\vec{r} - \vec{r}_C) \times \delta\vec{j}(\vec{r},\omega), \tag{3.58}$$

where $\delta\vec{j}(\vec{r},\omega)$ is the induced current density and $\delta\rho(\vec{r},\omega)$ is the induced density. In Eq. (3.57) we used the continuity equation, $\nabla\cdot\delta\vec{j}(\vec{r},\omega) = i\omega\delta\rho(\vec{r},\omega)$, and we restricted ourselves to systems in which charge is conserved. Therefore, while $\delta\vec{m}(\omega)$ depends on the choice for $\vec{r}_C$, $\delta\vec{p}(\omega)$ does not. The choice of $\vec{r}_C$ determines to what extent $\delta\vec{p}$ influences $\delta\vec{m}(\omega)$. Since $\vec{r}_C$ lies in the molecular frame, it ensures that $\delta\vec{m}(\omega)$ is independent of the choice of the origin of the coordinate system $\vec{r}_O$.

Due to Faraday's law, a homogeneous $\vec{B}(\omega)$ field is accompanied by a transverse electric field $\vec{E}^B(\vec{r},\omega)$ according to $\nabla\times\vec{E}^B(\vec{r},\omega) = i\omega\vec{B}(\omega)$. It can be written explicitly as

$$\vec{E}^B(\vec{r},\omega) = \frac{i\omega}{2}\vec{B}(\omega) \times (\vec{r} - \vec{r}_G), \tag{3.59}$$

where $\vec{r}_G$ is a fixed reference point in the molecular frame that guarantees that $\vec{E}^B(\vec{r},\omega)$ is independent of the choice of the origin of the coordinate system. It points to a position in the molecule where the electric field vanishes. The electromagnetic fields, $\vec{B}(\omega)$ and $\vec{E}^B(\vec{r},\omega)$, can be represented by the following transverse vector potential,

$$\vec{A}(\vec{r},\omega) = \frac{1}{2}\vec{B}(\omega) \times (\vec{r} - \vec{r}_G). \tag{3.60}$$

Since several $\vec{E}^B(\vec{r},\omega)$ correspond to the same $\vec{B}(\omega)$, both $\overleftrightarrow{\xi}$, and $\overleftrightarrow{G}$ depend on the particular choice for $\vec{E}^B(\vec{r},\omega)$. This dependence is physical since $\vec{E}^B(\vec{r},\omega)$ is fixed by the experimental setup. Instead, the uniform $\vec{E}(\omega)$ field in Eq. (3.56) can only be combined with a static $\vec{B}$ field already present in the ground state. Therefore $\overleftrightarrow{\tilde{G}}$ is independent of $\vec{E}^B(\vec{r},\omega)$. Without loss of generality, we consider a time-reversal symmetric ground state and we consider an external field for which only the j-th

component is nonzero. The magnetizability and optical rotation tensors then take the form:

$$\xi_{ij}(\vec{r}_C, [\vec{E}^B], \omega) = \frac{1}{2B_j(\omega)} \int d\vec{r} \left[(\vec{r} - \vec{r}_C) \times \delta\vec{j}(\vec{r}, \omega) \right]_i , \tag{3.61}$$

$$G_{ij}([\vec{E}^B], \omega) = \frac{i}{\omega} \frac{1}{B_j(\omega)} \int d\vec{r} \delta\vec{j}_i(\vec{r}, \omega), \tag{3.62}$$

$$\tilde{G}_{ij}(\vec{r}_C, \omega) = \frac{1}{2E_j(\omega)} \int d\vec{r} \left[(\vec{r} - \vec{r}_C) \times \delta\vec{j}(\vec{r}, \omega) \right]_i . \tag{3.63}$$

where the dependence on $\vec{r}_C$ and $\vec{E}^B$ have been made explicit. The above expression are independent of the choice of the origin of the coordinate system. Equations (3.61), (3.62) and (3.63) show that the induced current density is the fundamental quantity from which we can calculate $\overleftrightarrow{\xi}$, $\overleftrightarrow{G}$ and $\overleftrightarrow{\tilde{G}}$. Within the linear-response regime it is given by

$$\delta\vec{j}(\vec{r}, \omega) = \int d\vec{r}' \chi^{\vec{j}_p \vec{j}_p}(\vec{r}, \vec{r}', \omega) \cdot \vec{A}(\vec{r}', \omega) + \rho_0(\vec{r}) \vec{A}(\vec{r}, \omega), \tag{3.64}$$

where the first term on the right-hand side is the induced paramagnetic current ($\delta\vec{j}_p$) and the second term the induced diamagnetic current ($\delta\vec{j}_d$). Furthermore, $\rho_0(\vec{r})$ is the ground-state density and $\chi^{\vec{j}_p \vec{j}_p}(\omega)$ is the paramagnetic current-response function given by

$$\chi^{\vec{j}_p, \vec{j}_p}(\vec{r}, \vec{r}', \omega) = \lim_{\eta \to 0^+} \sum_n \langle \Psi_0 | \hat{\vec{j}}_p(\vec{r}) | \Psi_n \rangle \langle \Psi_n | \hat{\vec{j}}_p(\vec{r}') | \Psi_0 \rangle$$
$$\times \left[\frac{1}{\omega - (E_n - E_0) + i\eta} - \frac{1}{\omega + (E_n - E_0) + i\eta} \right], \tag{3.65}$$

where Ψ_n are the exact eigenstates and E_n the exact eigenvalues of the unperturbed Hamiltonian, η is an infinitesimal that ensures causality, and the paramagnetic current operator $\hat{\vec{j}}_p(\vec{r})$ is defined as $\hat{\vec{j}}_p(\vec{r}) = -\frac{i}{2} \sum_i (\nabla_{\vec{r}_i} \delta(\vec{r} - \vec{r}_i) + \delta(\vec{r} - \vec{r}_i) \nabla_{\vec{r}_i})$.

From Eq. (3.64) we see that the paramagnetic and diamagnetic currents are not treated on an equal footing. While the diamagnetic current only depends on the ground state, the paramagnetic current depends on all (ground and excited) states. The size of the basis set used determines not just the quality of the eigenstates but indirectly also the dimension of the excited-state space included in the sum-over-states expansion in Eq. (3.65). Therefore $\delta\vec{j}_p(\vec{r}, \omega)$ will converge much slower with the size of the basis set than $\delta\vec{j}_d(\vec{r}, \omega)$. The result is an incomplete cancelation of the gauge dependence of $\delta\vec{j}_p(\vec{r}, \omega)$ and $\delta\vec{j}_d(\vec{r}, \omega)$. Therefore an artificial dependence on $\vec{r}_G$ will arise in the calculation of the current density using a finite basis set. Let us illustrate this problem by looking at the limit $\omega \to 0$. In this limit the current density can be

written as

$$\delta\vec{j}(\vec{r},0) = \frac{1}{2}\Bigg\{ \int d\vec{r}' \overleftrightarrow{\chi}^{j_p j_p}(\vec{r},\vec{r}',0)\cdot\vec{B}(0)\times\vec{r}' + \rho_0(\vec{r})\vec{B}(0)\times\vec{r} - \underbrace{\left[\int d\vec{r}' \overleftrightarrow{\chi}^{j_p j_p}(\vec{r},\vec{r}',0) - \rho_0(\vec{r})\overleftrightarrow{\mathrm{I}}\right]}_{\neq 0 \text{ for finite basis set}} \cdot[\vec{B}(0)\times\vec{r}_G]\Bigg\} \tag{3.66}$$

where we used Eqs. (3.60) and (3.64). For a finite basis there is a linear dependence on $\vec{r}_G$ because the quantity within the square bracket does not vanish for a finite basis set.

The problem shown in Eq. (3.66) also suggests a solution. Since the exact current density is gauge invariant, *i.e.*, independent of $\vec{r}_G$, the quantity within the square brackets should be zero when a complete basis set is used. We obtain the following sum rule from this observation,

$$\rho_0(\vec{r})\delta_{ij} = \int d\vec{r}' \chi_{ij}^{j_p j_p}(\vec{r},\vec{r}',0). \tag{3.67}$$

In other words, integrating out one of the spatial variables of the paramagnetic current-density response function at $\omega = 0$ leads to a tensor with the ground-state density on its diagonal while its off-diagonal elements vanish. We can now use this sum rule to put $\delta\vec{j}_p(\vec{r},\omega)$ and $\delta\vec{j}_d(\vec{r},\omega)$ on equal footing by rewriting $\delta\vec{j}_d(\vec{r},\omega)$ as

$$\delta\vec{j}_d(\vec{r},\omega) = -\left[\int d\vec{r}' \chi^{\vec{j}_p\vec{j}_p}(\vec{r},\vec{r}',0)\right]\cdot\vec{A}(\vec{r},\omega). \tag{3.68}$$

We will call this relation the diamagnetic-current sum rule. We note that Eq. (3.67) can also be derived explicitly [53, 54]. We conclude that the diamagnetic current density can be exactly rewritten in terms of the static paramagnetic-current response function. The current density in Eq. (3.64) can therefore be rewritten according to

$$\delta\vec{j}(\vec{r},\omega) = \int d\vec{r}' \chi^{\vec{j}_p\vec{j}_p}(\vec{r},\vec{r}',\omega)\cdot\vec{A}(\vec{r}',\omega) - \left[\int d\vec{r}' \chi^{\vec{j}_p\vec{j}_p}(\vec{r},\vec{r}',0)\right]\cdot\vec{A}(\vec{r},\omega). \tag{3.69}$$

Using the diamagnetic-current sum rule in Eq. (3.68) for the diamagnetic current the total current in the limit $\omega \to 0$ is written as

$$\delta\vec{j}(\vec{r},0) = \frac{1}{2}\int d\vec{r}' \chi^{\vec{j}_p\vec{j}_p}(\vec{r},\vec{r}',0)\cdot\vec{B}(0)\times(\vec{r}'-\vec{r}), \tag{3.70}$$

which is independent of the gauge origin $\vec{r}_G$ as it should.

We applied this approach within time-dependent current-density-functional theory (TDCDFT) which is a numerically efficient approach to calculate the current density. We used the local-density approximation (LDA) in the ground-state calculation and the adiabatic local-density approximation (ALDA) for the response calculation. In Ta-

Table 3.5: Convergence behavior of the isotropic magnetizability (in a.u.) of C_2H_4 with the size of the basis set using the sum rule ($\xi(\omega)$) and without using the sum rule ($\tilde{\xi}(\omega)$). $\xi_p(=\tilde{\xi}_p)$ is obtained from the paramagnetic current while ξ_d and $\tilde{\xi}_d$ are obtained from the diamagnetic current.

Basis set	$\omega = 0$					$\omega = 0.07732$ a.u.	
	$\tilde{\xi}$	ξ	$\xi_p = \tilde{\xi}_p$	$\tilde{\xi}_d$	ξ_d	$\tilde{\xi}$	ξ
ASZ	-6.57	-3.22	7.41	-13.98	-10.63	-6.29	-2.91
ADZ	-6.39	-3.47	7.63	-14.02	-11.11	-6.10	-3.16
ADZP	-5.37	-4.14	8.58	-13.95	-12.72	-5.07	-3.80
ATZP	-5.29	-4.16	8.66	-13.95	-12.82	-4.98	-3.82
ATZ2P	-5.23	-4.12	8.65	-13.89	-12.77	-4.93	-3.79
QZ4P	-4.20	-4.16	9.66	-13.86	-13.82	-3.90	-3.83

ble 3.5 we report the convergence behavior of the isotropic magnetizability ($\xi(\omega)$) of C_2H_4 with the size of the basis set, using simple augmented basis sets[55] and the large QZ4P basis, for $\omega = 0$ and $\omega = 0.07732$ a.u. which is the sodium D-line frequency. We compare the results obtained using the current of Eq. (3.69) (labeled ξ) with those obtained using Eq. (3.64) (labeled $\tilde{\xi}$). We see that without using the diamagnetic-current sum rule convergence is extremely slow. Even for the ATZ2P basis [55] the values for $\tilde{\xi}$ are far from converged when we compare with the values obtained with the large QZ4P basis. Instead, the values for ξ are already converged to within 1% using an ADZP basis. This is true for both the static and the frequency-dependent magnetizability. Therefore, the reported values for the magnetizabilities in the remainder of this work are obtained with an ADZP basis set unless stated otherwise. We also report the paramagnetic and diamagnetic contributions to the magnetizability separately. They were obtained with the paramagnetic and diamagnetic current, respectively. We observe that the paramagnetic contribution converges slowly while the diamagnetic contribution obtained without sum rule converges rapidly. As a consequence, the to-

Table 3.6: Static isotropic magnetizabilities of various molecules (in a.u.). Comparison of the values obtained with our approach and LDA magnetizabilities reported in the literature. We also compare to experimental values.

Molecule	$\xi(\omega = 0)$		
	this work	other works	experiment
H_2O	-3.01	-3.05[56]	-2.76 ± 0.38[57]
NH_3	-3.73	-3.78[56]	-3.68 ± 0.38[58]
C_2H_4	-4.14	-4.20[56]	-4.23± 0.16[58]
Benzene	-11.70	-11.56[59]	-11.53 ± 0.13 [60]
Pentacene	-41.85	-	-40.56[61]

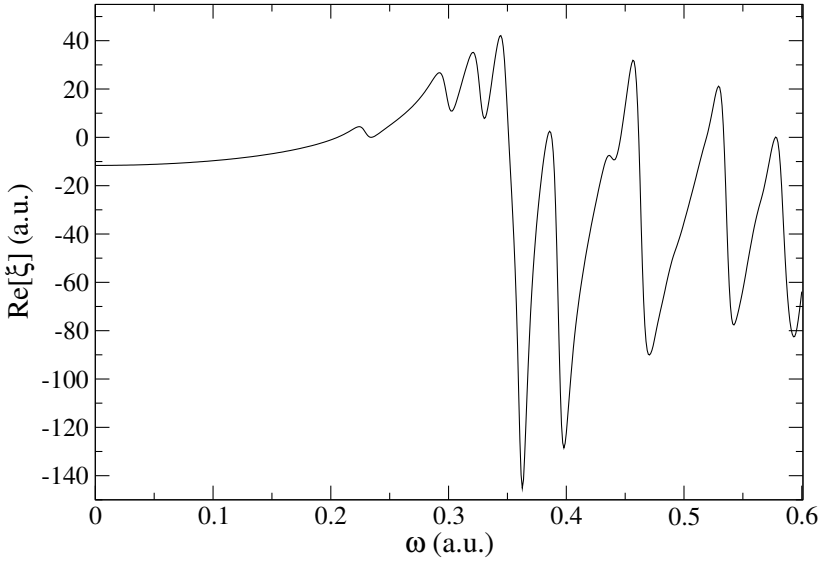

Figure 3.9: The real part of $\xi(\omega)$ for benzene.

tal magnetizability converges as slowly as the paramagnetic part. Instead, when we calculate the diamagnetic part using the sum rule both contributions converge equally slowly but with opposite sign. Therefore, thanks to a systematic error cancelation, the total magnetizability converges rapidly. Our converged value for the static magnetizability of C_2H_4 also compares well with a recently published value, *i.e.*, -4.20 a.u..[56]

In table 3.6 we show the static isotropic magnetizabilities of various molecules obtained with our approach and compare them to LDA magnetizabilities reported in the literature as well as to experimental values. We observe that our values are in good agreement with the magnetizabilities reported in the literature. As a proof of principle that with our approach we can calculate magnetizabilities over a wide range of frequencies, we plot in Fig. 3.9 the real part of $\xi(\omega)$ for benzene. To ensure that enough unoccupied orbitals are included to describe the high-frequency range we used a QZ4P basis set. We used a damping factor of 0.007 a.u.. Unfortunately, there is no experimental data is available to compare with.

Using the same approach we can calculate the optical rotation tensor from which circular dichroism (CD) spectra can be deduced. The CD spectrum for non-oriented systems can be obtained from the molar circular dichroism $\Delta\epsilon$ (in l mol^{-1}cm^{-1}) which is defined by

$$\Delta\epsilon(\omega) = 4.0712 \times 10^{-10}\bar{\nu}^2 \mathrm{Im}[\beta(\omega)] \;, \tag{3.71}$$

in which $\bar{\nu} = \omega/(2\pi c)$ is the wavenumber (in cm^{-1}). The optical rotation parameter $\beta(\omega)$ (in a.u.) is given by

$$\beta(\omega) = \frac{1}{3i\omega}\mathrm{Tr}[G] = -\frac{1}{3i\omega}\mathrm{Tr}[\tilde{G}]. \tag{3.72}$$

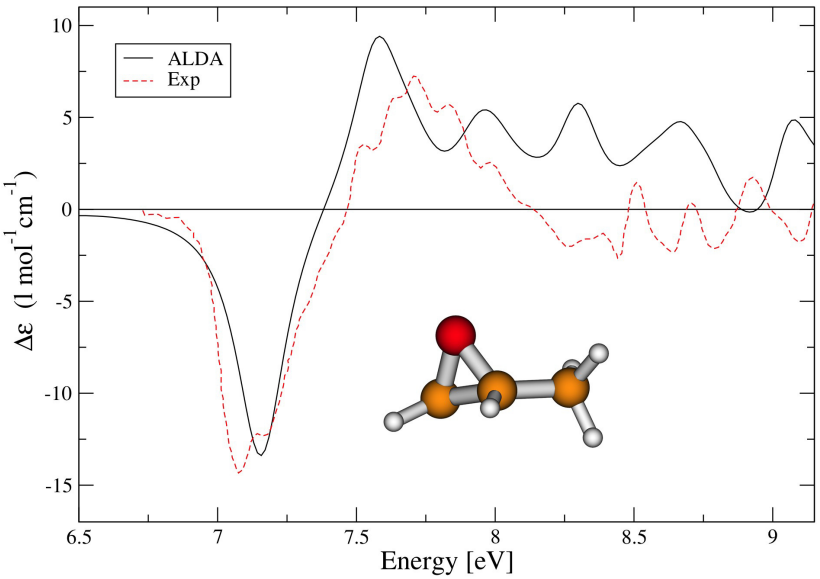

Figure 3.10: The circular dichroism spectra for R-methyloxirane. Solid line: ALDA; dashed line: experiment from Ref. [62]

We note that β does not depend on $\vec{r}_G$ nor $\vec{r}_C$ if Eq. (3.64) is used, even for a finite basis set, because it is proportional to the trace of G (or $\tilde{G}$). However, it suffers from the same slow convergence with basis-set size as the current density. The diamagnetic-current sum rule solves this problem.

In Figs. 3.10, 3.11, and 3.12 we compare our gauge-invariant CD spectra of R-methyloxirane, trans-2,3-dimethyloxirane (DMO), and α-pinene, respectively, with those obtained in experiment [62–64]. Since these experiments were done in the gas phase, the comparison is not hampered by effects due to the solvent. To facilitate comparison with experiment the theoretical results were blueshifted by 1.3 eV (R-methyloxirane), 1.25 eV (DMO) and 0.85 eV (α-pinene) and a damping of 0.1 eV (R-methyloxirane and DMO) and 0.2 eV (α-pinene) was used to simulate broadening effects in the experiment. We see that, in general, the ALDA circular dichroism spectra are in good agreement with those obtained in experiment. For R-methyloxirane the differences with experiment are mainly due to vibrational excitations which were not taken into account in the calculations. In the case of DMO the qualitative agreement with experiment is also good, but the quantitative discrepancy is not only due to the omission of vibrations. The spectrum could probably be improved by using a more accurate exchange-correlation functional, either in the response calculation or in the ground state (or both). In the case of α-pinene the agreement of the ALDA spectrum with experiment is excellent up to 7 eV and differences are mainly due to vibrations. For higher frequencies the quantitative agreement could also be improved by using a better functional. In Table 3.7 we report the specific rotations at the sodium D-line frequency ($[\alpha]_D$) for several molecules. We note that specific rotations are also implicitly contained in the CD spectra since the specific rotation is related

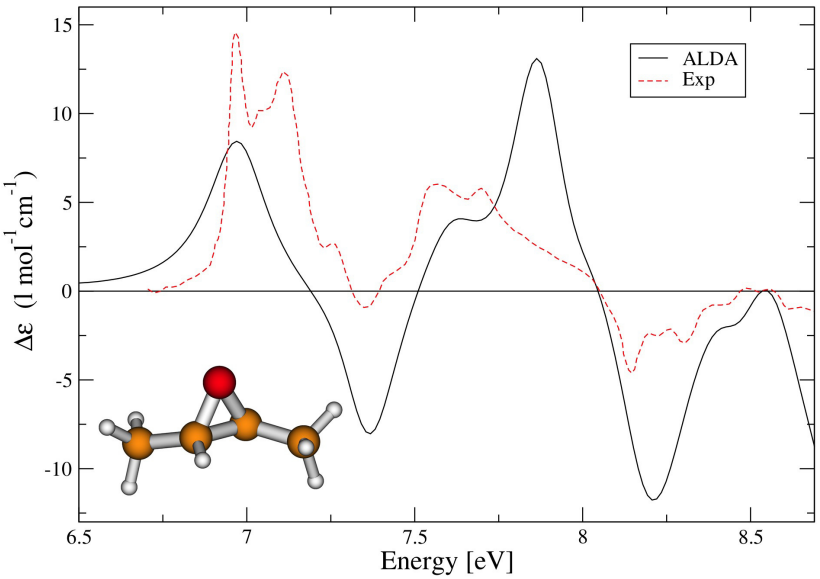

Figure 3.11: The circular dichroism spectra for DMO. Solid line: ALDA; dashed line: experiment from Ref. [63]

to the Kramers-Kronig transform of the CD spectra evaluated at a given frequency. We compare our results to the ALDA results reported in Ref. [65]. We see that, in general, our results are in good agreement with the values of Ref. [65]. Discrepancies may be due to the use of different geometries. We also compare to experimental values. There is a reasonable to good agreement with experiment with the exception of R-methyloxirane for which the ALDA gives a specific rotation that is much too small. It is important to note that, nevertheless, the CD spectrum of R-methyloxirane in Fig. 3.10 compares very well with experiment. Therefore we argue that the calculation of specific rotations should always be supplemented by CD spectra since the latter contain much more information. Finally, in Table 3.8 we demonstrate the fast

Table 3.7: Specific rotations at the sodium D-line frequency ($[\alpha]_D$) of several molecules calculated within the ALDA.

Molecule	$[\alpha]_D$		
	this work	other work [65]	experiment
R-methyloxirane	0.4	0.8	18.7 [66]
DMO	-65.9	-65.5	-58.8 [67]
trans-2,3-dimethylthiirane	141.8	125	129.0 [68]
3-methyl-cyclobutene	-189.8	-193.4	-176.0 [69]
trans-1,2-dimethylcyclopropane	-55.7	-56.8	-42.0 [70]
α-pinene	32.7	46.1	51.6 [71]
pentahelicene	-3246.2	-3007.5	-2160.0 [72]

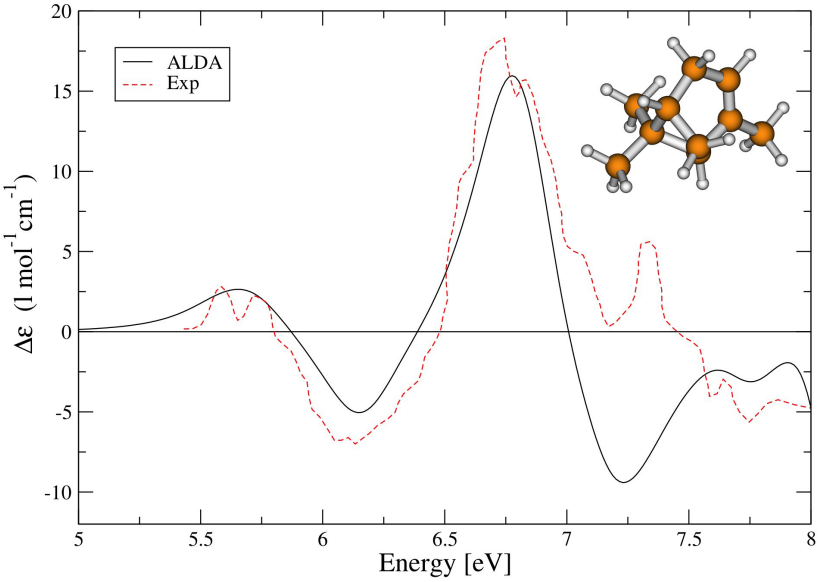

Figure 3.12: The circular dichroism spectra for α-pinene. Solid line: ALDA; dashed line: experiment from Ref. [64]

convergence of our method with the size of the basis set for a specific rotation of DMO and α-pinene. We compare results obtained with simple augmented basis sets[55] to a large even-tempered basis set (ET-QZ3P-3DIFFUSE).

In conclusion, we derived a simple framework to efficiently calculate gauge-invariant static and dynamical magnetic properties. Our method can be used in combination with any *ab initio* theory from which the current density can be obtained. We illustrated our approach by applying it to TD-current-DFT for the calculation of magnetizabilities and circular dichroism.

Table 3.8: Convergence with basis-set size of the specific rotation at the sodium D-line frequency ($[\alpha]_D$) for DMO and α-pinene.

Basis set	$[\alpha]_D$	
	DMO	α-pinene
ADZ	-58.4	16.1
ADZP	-68.3	27.0
ATZP	-61.3	30.9
ATZ2P	-61.0	32.3
ET-QZ3P-3DIFFUSE	-65.9	32.7

3.4 Unphysical and Physical Solutions in Many-Body Theories: from Weak to Strong Correlation

Many of the results obtained in the previous sections are the result of self-consistent-field (SCF) calculations in which the potentials depend on the quantity of interest and vice versa. However, in general, this constitutes a non-linear problem with more than one solution. These solutions might be physical but also unphysical. As a consequence, the result of an SCF approach will depend on the chosen iterative scheme. This raises the question which iterative scheme leads to a physical and which scheme to an unphysical solution. In this section we will address the general problem of multiple solutions for the one-body Green's function using a very simple model.

corresponding publications

- *Solution to the many-body problem in one point*
  J. A. Berger, P. Romaniello, F. Tandetzky, B. Mendoza, C. Brouder, and L. Reining
  New J. Phys. **16**, 113025 (2014)

- *Unphysical and Physical Solutions in Many-Body Theories: from Weak to Strong Correlation* A. Stan, P. Romaniello, S. Rigamonti, L. Reining, and J. A. Berger
  New J. Phys. **17**, 093045 (2015)

Many-body theories rely heavily on self-consistent equations that are constructed in terms of the physical quantities of interest themselves, such as the density or the Green's function. Consequently, the calculation of important properties such as total energies or photo-emission spectra requires the solution of nonlinear equations which have physical solutions but also unphysical solutions. Let us take the example of many-body perturbation theory (MBPT) [73], where the interacting Green's function G is given as a functional of the non-interacting Green's function G_0 and the bare Coulomb interaction v_c. An important idea of MBPT is to avoid a possibly ill-behaved perturbation expansion of G in terms of v_c and G_0 using Dyson equations. These are integral equations that describe the propagation of particles in terms of an effective potential or interaction. For the one-body Green's function, for example, this effective potential, which is the kernel of the Dyson equation, is the self-energy Σ. The power of this approach resides in the fact that even a low-order approximation for Σ yields contributions to all orders in v_c. Following Luttinger and Ward [74], Σ is usually expressed as a functional of G instead of G_0. However, this makes the Dyson equation non-linear, which leads to multiple solutions [75, 76]. This is a very fundamental and general problem. It is different from usual problems of convergence or local minima [77–80]. For example, convergence problems can be readily detected from the oscillatory

behavior of the results. The appearance of fully converged, but unphysical results, instead, is much more subtle and dangerous, and it has important consequences. It is the topic of this section.

To analyze the problem we use the so-called one-point model (OPM) [81–83]. This model is not system specific and can be solved exactly, such that the physical solution is well defined. It represents important structural aspects of the many-body problem, while collapsing all arguments of the Green's functions, self-energy, and the interaction to one point, making the equations scalar. In Ref. [75], an approximate version of the OPM was used to discuss multiple solutions within the framework of the *GW* approximation [9] to the self-energy.

In the present work we use the OPM without approximations, which simulates the full many-body problem. The exact OPM Green's function was derived in Ref. [84] from the one-point equivalent of the equation of motion of G, expressed as a functional differential equation [85]. The exact solution reads

$$y[y_0, u] = \frac{y_0}{1 + \frac{1}{2}uy_0^2} \quad \text{and} \quad \tilde{s}[y_0, u] = -\frac{1}{2}uy_0, \tag{3.73}$$

where y, y_0, and u represent G, G_0, and v_c, respectively. The self-energy $\tilde{s}$ is determined from the Dyson equation $\tilde{s}[y_0, u] = y_0^{-1} - y^{-1}[y_0, u]$. In Eq. (3.73) $\tilde{s}$ is given as a functional of the bare interaction u and the noninteracting Green's function y_0. Usually, however, one works with the self-energy given as a functional of the dressed Green's function, $s[y, u]$. Then the Dyson equation reads

$$y = y_0 + y_0 s[y, u] y. \tag{3.74}$$

This is, in general, a non-linear equation. We first consider the HF self-energy, which in the OPM is $s^{\mathrm{HF}}[y, u] = -\frac{1}{2}uy$. Let us look at the map $G_0 \to G$, *i.e.*, the usual case, where y_0 is set by the system, and one searches y. The Dyson equation has two solutions,

$$Y^{\pm}_{\mathrm{HF}} = \frac{1}{V}\left[-1 \pm \sqrt{1 + 2V}\right], \tag{3.75}$$

with the rescaled quantities $Y = y/y_0$ and $V = uy_0^2$. Here Y^{+}_{HF} is the physical solution, since it connects smoothly to $Y_0 = 1$ at $V = 0$, and Y^{-}_{HF} is an unphysical solution, that diverges for vanishing interaction. Both are shown in the inset of Fig. 3.13. In real problems Dyson equations are solved iteratively. Two possible iteration schemes are:

$$Y^{(n+1)} = \frac{2}{2 + VY^{(n)}} \ (\mathbf{I}); \ Y^{(n+1)} = \frac{2}{VY^{(n)}} - \frac{2}{V} \ (\mathbf{II}). \tag{3.76}$$

While neither of the two schemes has convergence problems when iterating, only scheme (**I**) converges to the physical solution, whereas scheme (**II**) converges to the unphysical solution. This happens because the iteration leads to the continued fraction representation of the square root [75] in Eq. (3.75),

$$\sqrt{1 + x} = 1 + \frac{x/2}{1 + \frac{x/4}{1 + \frac{x/4}{1 + \cdots}}}, \tag{3.77}$$

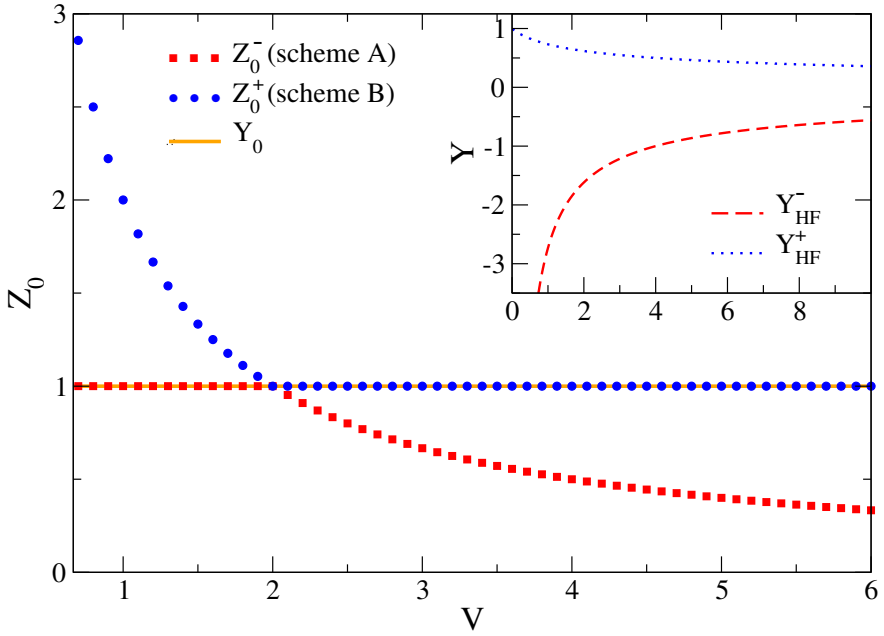

Figure 3.13: One-point model (OPM): $Z_0^{\pm}$ as a function of the interaction V. Squares (red): Z_0^- and solution of scheme (**A**); circles (blue): Z_0^+ and solution of scheme (**B**); continuous line (orange): the exact solution Y_0. Inset: $Y_{\rm HF}^{\pm}$ as a function of the interaction V.

for $x = 2V$. The sign of the square root is determined by the continued fraction in the iterative procedure.

So far we have looked at the map $G_0 \to G$. We now focus on the inverse map $G_0 \leftarrow G$. This map is needed in problems of embedding, where one optimizes an auxiliary quantity G_0 in order to produce certain properties of a real system (contained in G). The inverse map is also crucial when one wants to express a functional in terms of dressed instead of bare quantities. The most prominent example is the Luttinger-Ward (LW) functional, where the self-energy is given in terms of G instead of G_0 [74, 86–88]. For the LW functional to be properly defined, the map $G_0 \leftarrow G$ should be unique.

Within the OPM, consider a system with the bare Green's function y_0, and with the exact, interacting Green's function y given by Eq. (3.73). We now fix y and examine whether the inverse map $z_0 \leftarrow y$ unambiguously leads to $z_0 = y_0$. With the exact self-energy $\tilde{s}[z_0] = -\frac{1}{2}uz_0$ of Eq. (3.73), the exact Dyson equation of this problem reads

$$z_0 = y + \frac{1}{2}uyz_0^2, \tag{3.78}$$

in which y is known and z_0 is to be determined. This equation has again two solutions:

$$z_0^{\pm} = \frac{1}{uy}\left(1 \pm \sqrt{1-2uy^2}\right) \Rightarrow Z_0^{\pm} = \frac{2+V \pm \sqrt{(2-V)^2}}{2V}, \tag{3.79}$$

where $Z_0 = z_0/y_0$ and we used Eq. (3.73). The square root in Eq. (3.79) equals the

absolute value $|2-V|$. Because $2-V$ changes sign at $V=2$, the physical solution $Y_0=1$ is obtained by Z_0^- for $V<2$ and by Z_0^+ for $V>2$ (see Fig. 3.13). In other words neither of the two solutions gives $Z_0=Y_0$ for all V. As a consequence *one has to change sign in front of the square root* in Eq. (3.79) at $V=2$. This has important consequences for the iterative solution of Eq. (3.78): because scheme (**I**) yields the square root with positive sign, to obtain the map $G_0 \leftarrow G$ we need *two different iteration schemes*: one for $0<V<2$ and the other for $V>2$. This is different from the map $G_0 \rightarrow G$, where one solution gives the physical solution for all V, and hence a single iteration scheme suffices.

The need to change iteration scheme is a serious problem. Indeed, Kozik *et al.* [89] pointed out that different iteration schemes, applied to Hubbard and Anderson models, lead to different solutions which cross at a certain interaction. Our OPM results provide the missing explanation: keeping the labels (**A**) and (**B**) of [89], the two iteration schemes correspond to

$$\frac{1}{Z_0^{(n+1)}} = 1+\frac{1}{2}V(1-Z_0^{(n)}) \qquad (\mathbf{A}), \tag{3.80}$$

$$\frac{1}{Z_0^{(n+1)}} = -1-\frac{1}{2}V(1-Z_0^{(n)})+\frac{2}{Z_0^{(n)}} \quad (\mathbf{B}). \tag{3.81}$$

We report the results in Fig. 3.13. Scheme (**A**) converges to the physical solution for $V<2$ and to the unphysical solution for $V>2$. Instead, scheme (**B**) converges to the unphysical solution for $2/3<V<2$ and to the physical solution for $2<V<6$. These results are strictly analogous to those obtained by Kozik *et al.* for Hubbard and Anderson models. They can be understood from the fact that scheme (**A**) creates a continued fraction with positive square root, whereas in scheme (**B**) the sign of the continued fraction is changed.

This sign problem is *a priori* a disaster because there is no unique prescription of how to avoid unphysical solutions. The OPM highlights the reducible polarizability [84]

$$\frac{\chi}{\chi_0} = 2\frac{2-V}{(2+V)^2}, \tag{3.82}$$

as critical quantity that changes sign at the crossing $V=2$. At the same time, for $V>2$ the perturbation expansion of y, in Eq. (3.73), diverges. Our result indicates that one should in principle inspect the exact two-particle correlation function as a function of the interaction to detect problems of perturbation theory. This is in line with Ref. [90] in which a breakdown of perturbation theory is linked to an eigenvalue of the two-particle correlation function that crosses zero, becoming negative.

Inverting a map between functionals requires a careful definition of their domain [91, 92]. The multiple solutions are the price to pay for the fact that we have not considered this definition in the above discussion. For a system with a non-degenerate ground state this can be understood as follows: if there were two solutions for $G_0 \leftarrow G$,

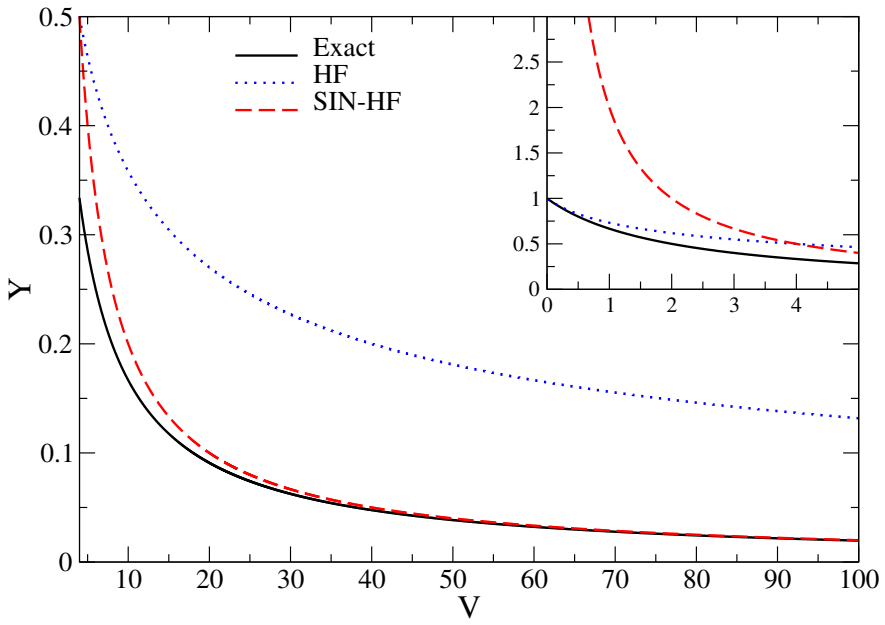

Figure 3.14: One-point model (OPM): Y as a function of the interaction V for $4 < V < 100$. Solid line (black): exact solution; dotted line (blue): Hartree-Fock (HF); dashed line (red): strong-interaction HF (SIN-HF). Inset: Y as a function of V for $0 < V < 5$.

one could obtain the same dressed Green's function from two different G_0 and, hence, from two different external potentials. Since the diagonal of G is the density, the Hohenberg-Kohn theorem [1] states that there can only be one external potential, and hence one G_0, corresponding to each G. This means that any additional solution G_0 is unphysical, in the sense that it cannot be constructed from the solution of a one-body Schrödinger equation. Equivalently, it cannot be written as a sum of simple poles, each with a strength normalized to one. By imposing this condition, one can therefore eliminate unphysical solutions. In the OPM this trivially corresponds to the requirement $Z_0 = 1$, which already implies the solution. A more general discussion on the definition of the domain can be found in Ref. [92]. It should be noted that when G_0 is an embedding Green's function the discussion is more complicated, because one searches for a fictitious G_0 with a frequency dependence that can differ from that of a G_0 resulting from a static potential.

With the map $G_0 \leftarrow G$ one can construct the exact self-energy as a functional of G. Using Eq. (3.79) in the exact self-energy given in Eq. (3.73) we obtain

$$s^{\pm}[y,u] = -\frac{1}{2y}\left(1 \pm \sqrt{1-2uy^2}\right) \tag{3.83}$$

$$= -\frac{1}{2y} \mp \frac{1}{2y} \pm \frac{1}{2}u\left[y + \frac{uy^3}{2} + \frac{u^2y^5}{2} + ...\right]. \tag{3.84}$$

We note that the Luttinger-Ward functional in Eq. (3.83) is unique, but in order to calculate it one has to change the sign. The Dyson equation with the two self-energies

of Eq. (3.83) leads to two different Green's functions: the physical solution given in Eq. (3.73) is obtained from s^- for $V < 2$ and from s^+ for $V > 2$, and $y = 0$ from s^+ for any V. Therefore, for weak interaction using the exact self-energy one obtains only one solution, the physical one, contrary to, *e.g.*, the HF approximation. We note that at the point where s^+ and s^- meet (at $V = 2$) the derivative $ds^\pm/dy$ diverges. This could explain the divergence of $\delta\Sigma/\delta G$ observed in Ref. [90] in the paramagnetic DMFT solution of a Hubbard model. Note that this divergence occurs at the point where one of the eigenvalues of the polarizability crosses zero.

In Eq. (3.84) we Taylor expanded the square root. The convergence radius is infinite, since $0 \leq 2uy^2 \leq 1$, as can be shown using Eq. (3.73). Interestingly, the sum of the first two terms in (3.84) (upper sign) is the first term of an expansion of the self-energy for strong interaction [75]. The remaining terms constitute an expansion in terms of a quantity that is proportional to u and converges for all physical y. This means that one can use perturbation theory over the whole interaction range, but in two different ways for the two different regimes. To lowest order, this corresponds to HF, $s^{\mathrm{HF}} = -\frac{1}{2}uy$, for weak interaction, and $s^{\mathrm{SIN-HF}} = -\frac{1}{y} - s^{\mathrm{HF}}$, for strong interaction. We call this functional *strong-interaction HF* (SIN-HF). Both self-energies yield two solutions. We report the physical solution for these two approximations in Fig. 3.14. While HF clearly fails for strong interaction, SIN-HF is exact in the strong interaction limit and performs well for $V > 4$, while it is worse than HF for $V < 4$. It is important to note that the physical SIN-HF solution is obtained for $V > 1$ with the iteration scheme $1/Y^{(n+1)} = 1/Y^{(n)} + \frac{1}{2}VY^{(n)} - 1$. Indeed, the appropriate iteration scheme depends on the formulation of the problem. We suggest the OPM as a powerful tool to examine which scheme one should use for a given problem and interaction range.

To summarize, we have demonstrated that with a simple but general one-point model one can understand and solve structural problems of many-body perturbation theory. In particular, one can use it sort out the multiple solutions of the non-linear Dyson equation by choosing the appropriate iteration scheme. We have shown that for the map $G_0 \to G$ a single iteration scheme suffices to obtain the physical solution for all interaction strengths. Instead, for the inverse map $G_0 \leftarrow G$ one has to change iteration scheme at the interaction strength at which the reducible polarizability changes sign and perturbation theory of G in terms of G_0 starts to diverge. Nonetheless, we have proved that even for strong interaction one can use a perturbative expression for the self-energy in terms of G, which differs from the usual LW functional.

Chapter 4

Projects

In this last chapter I will present some of the projects planned for the coming years. I will focus on the projects for which funding has been received (section 1), confirmed (section 2) or requested (section 3), since these projects will have the priority. In section 4.1 I will discuss a natural continuation of the research described in section 3.3 where we proposed an efficient way to calculate magnetic response properties of molecules. We would like to extend this approach to extended systems described by periodic boundary conditions. The project in section 4.2 is a continuation of the developments described in section 4.1. Its goal will be to predict topological insulators from the magnetic response of a solid due to an electric field. Finally, in section 4.3 we will outline a project to describe resonant inelastic x-ray scattering (RIXS).

4.1 The magnetization of a periodic solid

In section 3.3 we developed a general approach to describe magnetic properties of finite systems. The aim of this project will be to extend the theory developed for finite systems to extended systems.

For the description of extended systems it is convenient to apply periodic boundary conditions (PBC). However, when using PBC, the polarization and the magnetization can no longer be defined as dipole moments per unit volume because the position operator that appears in the standard definitions of the electric and magnetic dipole moments, *i.e.*,

$$\vec{p}(t) = \int d\vec{r}\vec{r}\rho(\vec{r},t) \tag{4.1}$$

$$\vec{m}(t) = \frac{1}{2}\int d\vec{r}\vec{r}\times\vec{j}(\vec{r},t), \tag{4.2}$$

is not well defined in the thermodynamic limit. Moreover, using PBC, the surface of the system is artificially removed, which complicates the description of induced fields due to a surface density (polarization) or a surface current (magnetization) . These surface densities are themselves due to the reaction of the system to the external field (see Figs. 4.1 and 4.2). The description of the induced fields is still possible, but only if the surface effects can be described in terms of quantities related to the bulk material. For example, we can show that in the case of polarization the effects of charges accumulated on the surface can be expressed in terms of the current density in the bulk material using the continuity equation for the density $\rho(\vec{r},t)$,

$$\frac{\partial}{\partial t}\rho(\vec{r},t) + \nabla\cdot\vec{j}(\vec{r},t) = 0. \tag{4.3}$$

With this equation we can transform the expression for the electric dipole moment in

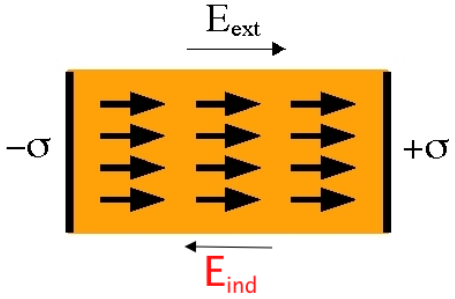

Figure 4.1: An external electric field $\vec{E}_{ext}$ is applied to a sample. As a result, the electrons will move and create a charge defect $(-\sigma)$ on one side of the sample, and a charge excess $(+\sigma)$ on the opposite side. This difference in potential induces an electric field $\vec{E}_{ind}$ which is opposite to the external field.

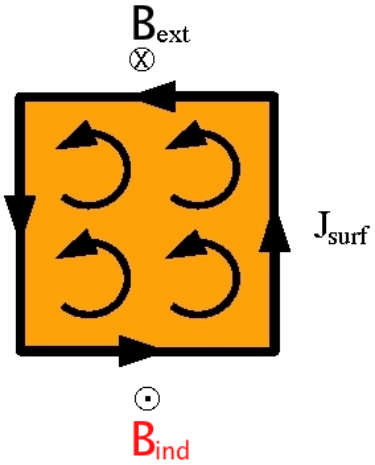

Figure 4.2: An external magnetic field $\vec{B}_{ext}$ is applied to a sample. As a result, the electrons will move and create a current density $\vec{j}_{surf}$ on the surface. The latter then induces a magnetic field $\vec{B}_{ind}$ which is opposite to the external field.

terms of the current of the bulk material:

$$\vec{p}(t) = \int d\vec{r}\vec{r}\rho(\vec{r},t) = \int_{t_0}^{t} dt' \int d\vec{r}\vec{j}(\vec{r},t'), \tag{4.4}$$

where for simplicity we assumed that $\vec{p}(t_0) = 0$. This allows us to define the polarization $\vec{P}(t)$ in extended systems as

$$\vec{P}(t) = \frac{1}{V}\int_{t_0}^{t} dt' \int_{V} d\vec{r}\vec{j}(\vec{r},t'), \tag{4.5}$$

with V the volume of a unit cell. Therefore, knowledge of the current density in a unit cell is sufficient to calculate the polarization. The current can be obtained from many approaches, an efficient method to obtain the current density is time-dependent current-density-functional theory (TDCDFT). This is the approach we used in section 3.2 to evaluate the macroscopic polarization of solids from which we obtained optical absorption spectra.

The problem is more complicated in the case of the magnetization where there is a surface current (see Fig. 4.2). Several solutions have been proposed, but these approaches only deal with systems that are described by a one-body Hamiltonian [93–97]. We want to have a general description that is also valid for many-body systems. Moreover, we would like to determine the bulk quantity that is sufficient to calculate the magnetization, *i.e.*,, the equivalent of the bulk current density in the case of the polarization. With this local bulk quantity we can formulate an efficient density-functional type of approach.

The strategy we will use in this project is similar to that used for the polarization because we will start from the general definition given in Eq. (4.2) for the magnetic

dipole moment. However, instead of using a continuity equation we will evaluate the current density as the expectation value of the the many-body current operator which is defined as

$$\hat{\vec{j}}(\vec{r}) = \frac{1}{2}\sum_i [\vec{v}(\vec{r}_i)\delta(\vec{r}-\vec{r}_i) + \delta(\vec{r}-\vec{r}_i)\vec{v}(\vec{r}_i)], \tag{4.6}$$

where $\vec{v}(\vec{r}_i) = -i[\vec{r}_i, \hat{H}]$ is the velocity operator with $\hat{H}$ the many-body Hamiltonian of the system. We can arrive at an expression for the magnetic dipole moment that is independent of the position operator by inserting a complete set of states in Eq. (4.2) and using the following identity

$$\langle \Psi_0 | \vec{r}_i | \Psi_n \rangle = i \frac{\langle \Psi_0 | \vec{v}(\vec{r}_i) | \Psi_n \rangle}{E_n - E_0} \qquad E_n \neq E_0, \tag{4.7}$$

in which $|\Psi_n\rangle$ are many-body states and E_n their corresponding energies, *i.e.*, the eigenstates and eigenvalues of $\hat{H}$. The resulting expression will be general and can be applied to both open and periodic boundary conditions.

Preliminary investigations seem to indicate that to obtain a correct expression for the magnetization at zero temperature T we have to take the expectation value of the current operator at finite temperature within the grand canonical ensemble and then take the limit $T \to 0$, instead of working from the start at $T = 0$.

4.2 Topological phase prediction from the magneto-electric effect

The project described in this section aims to provide a theory and a numerical tool for the prediction of topological insulators from first principles. The phase of an insulator (ordinary or topological) can be determined from the orbital magnetic polarizability which is the response function related to the polarization induced by a magnetic field. Experimentally topological phases have already been determined in this way, but there is no first-principles theory available to predict these phases. The goal of this project is to fill this gap by using linear-response theory to formulate a general expression for the calculation of the orbital magnetic polarizability in bulk systems described by periodic boundary conditions.

A topological insulator (TI) is a material that is insulating in its interior but has exotic conducting states on its surface. As a consequence electrons can only circulate along the surface of a TI. More importantly, the conducting surface states are topologically protected, which means that they are insensitive to the scattering by (nonmagnetic) impurities on the surface. This feature makes TI's a promising candidate for the discovery of novel phases with possible applications in spintronics and quantum computing. Topological insulators have recently attracted much attention, in particular thanks to the Nobel Prize which was awarded last year to Thouless, Haldane and Kosterlitz for theoretical discoveries of topological phase transitions and topological phases of matter [1]. There have already been several experimental realizations of TI's, see, for example, Refs. [98, 99]. A schematic representation of the band structure of a TI is given in Fig. 4.3. Although there are some features which are thought to be important for a material to have a topological phase, in particular strong spin-orbit coupling, there is no recipe that tells us whether a material has a topological phase or not. Therefore, it is important to search for possible indicators

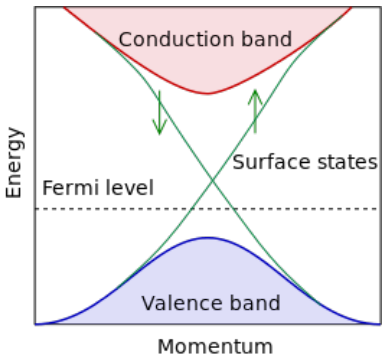

Figure 4.3: (source: wikipedia): Schematic representation of the band structure of a topological insulator. The band gap of the bulk states is crossed by surface states which are topologically protected

of topological phases.

A phase of matter can be defined as the response of a system with respect to an external perturbation. For example, a metal has a non-zero conductivity in response to an applied external field at low temperature. The pertinent response quantity to distinguish an ordinary insulator from a topological insulator can be obtained using so-called axion electrodynamics in which the usual Maxwellian Lagrangian is supplemented by the scalar product of the electric and the magnetic field, *i.e.*, $\vec{E} \cdot \vec{B}$ [100]. The coefficient that corresponds to this additional term is called the axion angle and has only two values that are compatible with time-reversal symmetry; it is either zero, which corresponds to an ordinary insulator, or it is equal to π, which indicates a (strong) topological insulator.

How can the axion angle be measured or calculated?

The axion angle can be linked to the magneto-electric polarizability which is the response function of the magneto-electric effect in which an applied electric field generates a magnetic field or vice versa. In the case of a TI one also speaks of the topological magneto-electric effect (TME). The axion angle is therefore also referred to as the orbital magnetic polarizability angle. Thus, from the measurement or calculation of the magneto-electric polarizability one can deduce the axion angle and therefore determine the topological phase. Experimentally this has already been realized; optical measurements can be used to identify topological insulators [101, 102]. Our goal is to provide the missing first-principles theory and computational tool.

Current first-principle tools focus solely on the calculation of the band structure to identify possible topological insulators. While a normal insulator has an *s*-like conduction band above the *p*,*d*-like valence bands, a topological insulator has an s-like conduction band below the *p*,*d*-like valence bands [103]. For this reason one says that TI's exhibit band inversion since the usual band order of normal insulators is inverted in TI's. However, the band inversion only establishes that there is a gapless state at the surface but it does not guarantee that the surface conduction states are topologically protected, and therefore insensitive to impurities. It is therefore a necessary condition but it is not a sufficient condition for the determination of a TI.

Besides this fundamental problem there are also several other disadvantages related to the determination of TI's through band structure calculations. Thanks to its numerical efficiency theoreticians mainly use Kohn-Sham density-functional theory (KS-DFT) to calculate the band structure of a material. However, the Kohn-Sham band structure is not equal to the true band structure, not even in principle. KS-DFT has led to many false positives when applied to the prediction of TI's [103]. The false positives were discovered by performing accurate many-body calculations to obtain the band structure. Unfortunately, these calculations are only possible for systems with few electrons due to the their large numerical cost.

In this project, we therefore propose to calculate directly the appropriate response

function, *i.e.*, the (topological) magneto-electric polarizability, from which the axion angle can be obtained. To achieve this goal we we will

1. Formulate a general theory for its calculation. Currently an explicit expression has only been derived for systems of noninteracting electrons [104, 105]. Such a general expression can be obtained from linear-response theory since the axion angle is related to the orbital magnetic polarizability which is a linear-response quantity. We will take particular care to ensure that this expression only contains bulk quantities, *i.e.*, quantities that are consistent with periodic boundary conditions (PBC). This is crucial since solids are most efficiently described within PBC. This problem is related to the one described in the previous section.

2. Validate this new expression by first applying it to the Fu-Kane-Mele model [106] which models a topological insulator on a diamond lattice and compare our results to those in the literature.

3. Implement our theory in a first-principles computer code that is already capable of calculating linear-response quantities. We will test our this numerical tool on materials which have experimentally been shown to be TI's. The numerical tool thus obtained can then be used for the prediction of new TI's.

4.3 Theoretical description of resonant inelastic x-ray scattering

The aim of this project is to develop the theory and software for the predictive description of Resonant Inelastic X-ray Spectroscopy (RIXS), an important experimental tool to probe elementary excitations in solids.

The elementary excitations contain the signature of many physical and chemical properties of materials and hence are key quantities for the comprehension of a system. Understanding an excitation spectrum of a material means understanding the material. The great technological advances of the ultimate-generation synchrotron radiation facility, giving high brilliance light in the ultraviolet, soft- and hard-x-rays regions, coupled with extremely tunable beams, makes it nowadays possible to measure directly the excitation spectrum of solids by means of Resonant Inelastic X-ray Scattering (RIXS). RIXS is an emerging technique that has encountered remarkable progress in the last decade thanks to its unique capability of probing the energy spectrum of elementary excitations and their dispersion in the reciprocal space [107]. The physical picture of RIXS can be summarized as follows (see Fig. 4.4): i) an incoming photon promotes a core electron to an empty conduction state; ii) a different electron from the valence region decays and annihilates the core hole. The net result is a final state with an electron-hole excitation, whose energy and momentum are defined by the conservation laws.

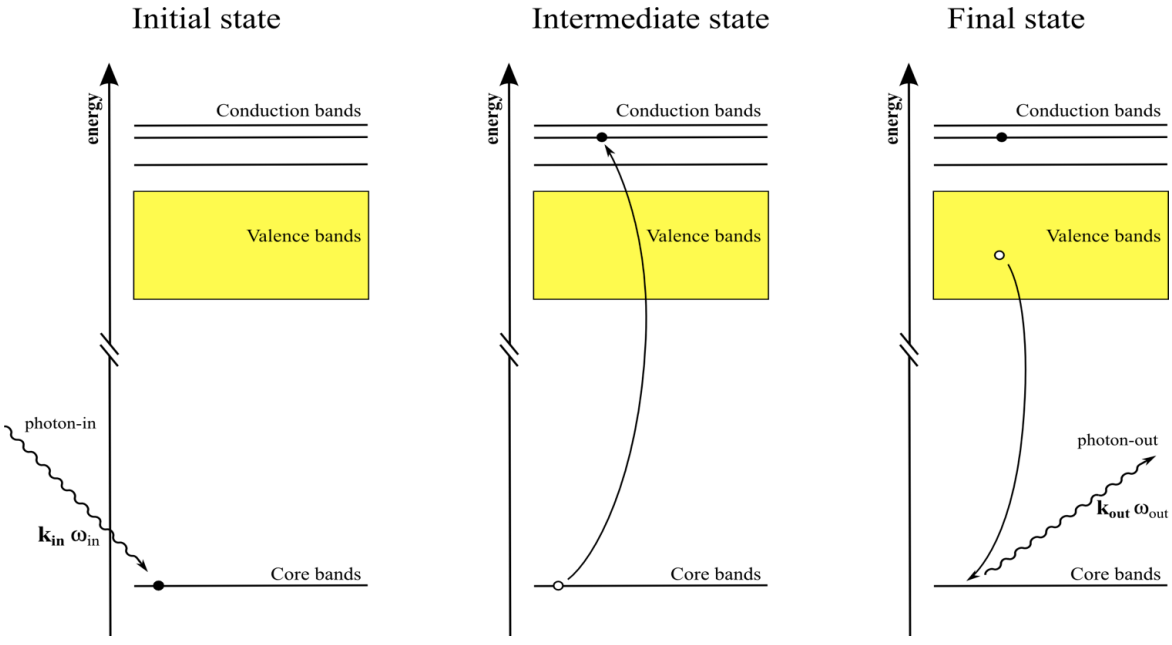

Figure 4.4: The RIXS process. Left and middle panel: an incoming photon promotes a core electron to an empty conduction state; right panel: a different electron from the valence region decays and annihilates the core hole.

Compared to other spectroscopic techniques, RIXS has numerous advantages, namely: huge scattering phase-space, bulk sensitivity, chemical specificity, polarization sensitivity and small sample volumes. Moreover, thanks to the technological improvement in the fabrication of high quality optics as well as the strong interest of the scientific community, RIXS experiments have recently reached high energy and momentum resolution. This is a great advantage, but also implies huge interpretation problems, as many elementary excitations participate and compete in the RIXS process. Therefore, without a powerful analysis tool, capable of disentangling different contributions present in one RIXS spectrum, the interpretation, analysis and, ultimately, the prediction of experiments remain strongly limited.

In this project we will develop a numerical tool for the theoretical description of RIXS. This will give an essential contribution to the analysis of the complex spectra of this emerging technique for probing elementary excitations in solids. Moreover, since the method is *ab initio*, it will be possible to apply it to any material and do predictive calculations. In particular, the theory will be able to describe the so-called strongly correlated materials, for which a wealth of RIXS data have been collected due to the variety of remarkable phenomena that these materials exhibit, *e.g.*, phase transitions with resistivity changes of many order of magnitude [108], *e.g.*, in vanadates, huge volume variations [109], *e.g.*, in cerium or plutonium, high Tc superconductivity [110], *e.g.*, in cuprates, or colossal magnetoresistence [111, 112], *e.g.*, in manganites, etc. Moreover, by assembling different strongly correlated electronic systems one can create new materials with novel properties. RIXS gives vital information about the (strong) electron correlation. However, the interpretation is very indirect and an accurate theory is needed in order to unravel the complex physics.

Unfortunately, the currently available methods are not sufficiently accurate to correctly describe RIXS. To arrive at a method that gives a saTI'sfactory description of RIXS spectra, some of the challenges we face are:

1. The accurate description of the resonant scattering amplitudes.

2. The coupling of different energy ranges. Contrary to, for example, ARPES (Angle Resolved Photo-Emission Spectroscopy), in a RIXS experiment the coupling between the high-energy range (in the photon-in and photon-out processes) and the low-energy range (final electron-hole state, intermediate screening effects due to the core-hole) is inextricable. It is crucial to be able to treat this coupling correctly.

3. The *ab initio* description of electron correlation. The challenge is to describe both weak-correlation phenomena such as screening as well as strong correlation which is present in many materials of technological interest.

In order to simulate the RIXS spectra we have to describe the electron-hole interactions of the intermediate and final states. We will use the Bethe-Salpeter equation

(BSE) [20], an *ab initio* theory that describes electron-hole interactions in absorption spectra. The project can thus be divided in the following two parts:

1. *The generalization of the Bethe-Salpeter equation to RIXS.*
   The starting point will be the Bethe-Salpeter equation (BSE) that describes the interaction between an electron promoted to a conduction band and the hole it leaves behind. It can hence be used to describe the interaction between the core hole and the excited electron in the intermediate state as well as the interaction between the valence hole and the excited electron in the final state of a resonant inelastic x-ray process (see Fig. 4.4). Up to now the BSE is almost exclusively used to describe optical absorption processes, which involves low-energy photons and zero momentum transfer. Recently, it has been extended to finite momentum transfer [**?**]. The first step is, therefore, to extend both the theory and the implementation of the BSE to the calculation of RIXS spectra, which require the description of high-energy photons and non-zero momentum transfer.

2. *The accurate description of electron correlation.*
   Correlation is the key for understanding the properties of many materials that exhibit a complex and technological interesting physics. The current approximations to correlation in BSE take into account screening effects but not the strong correlation between localized electrons. In order to accurately describe RIXS experiments for strongly correlated systems we will benefit from a recent method based on density matrices developed by us that gives qualitatively correct band structures of strongly correlated materials [113]. This will allow us to study materials, such as NiO [113] and V_2O_3 [114], for which standard approximations are not sufficient.

Bibliography

[1] P. Hohenberg and W. Kohn. Inhomogeneous electron gas. *Phys. Rev.*, 136:B864–B871, Nov 1964.

[2] X. Gonze, Ph. Ghosez, and R. W. Godby. Density-polarization functional theory of the response of a periodic insulating solid to an electric field. *Phys. Rev. Lett.*, 74:4035–4038, May 1995.

[3] Erich Runge and E. K. U. Gross. Density-functional theory for time-dependent systems. *Phys. Rev. Lett.*, 52:997–1000, Mar 1984.

[4] G. Vignale and Mark Rasolt. Density-functional theory in strong magnetic fields. *Phys. Rev. Lett.*, 59:2360–2363, Nov 1987.

[5] Asish K. Dhara and Swapan K. Ghosh. Density-functional theory for time-dependent systems. *Phys. Rev. A*, 35:442–444, Jan 1987.

[6] S. K. Ghosh and A. K. Dhara. Density-functional theory of many-electron systems subjected to time-dependent electric and magnetic fields. *Phys. Rev. A*, 38:1149–1158, August 1988.

[7] Giovanni Vignale. Mapping from current densities to vector potentials in time-dependent current density functional theory. *Phys. Rev. B*, 70:201102, Nov 2004.

[8] W G Aulbur, L Jönsson, and J W Wilkins. Quasiparticle calculations in solids. In *Solid State Physics*, volume 54, page 1. Academic, New York, 2000.

[9] Lars Hedin. New method for calculating the one-particle green's function with application to the electron-gas problem. *Phys. Rev.*, 139(3A):A796–A823, Aug 1965.

[10] J. A. Berger, Lucia Reining, and Francesco Sottile. Efficient *GW* calculations for SnO_2, ZnO, and rubrene: The effective-energy technique. *Phys. Rev. B*, 85:085126, Feb 2012.

[11] Fabien Bruneval, Nathalie Vast, and Lucia Reining. Effect of self-consistency on quasiparticles in solids. *Phys. Rev. B*, 74(4):045102, Jul 2006.

[12] Fabien Bruneval and Xavier Gonze. Accurate *GW* self-energies in a plane-wave basis using only a few empty states: Towards large systems. *Phys. Rev. B*, 78(8):085125, 2008.

[13] Bi-Ching Shih, Yu Xue, Peihong Zhang, Marvin L. Cohen, and Steven G. Louie. Quasiparticle band gap of zno: High accuracy from the conventional G^0W^0 approach. *Phys. Rev. Lett.*, 105(14):146401, Sep 2010.

[14] Christoph Friedrich, Mathias C. Müller, and Stefan Blügel. Band convergence and linearization error correction of all-electron *GW* calculations: The extreme case of zinc oxide. *Phys. Rev. B*, 83(8):081101(R), Feb 2011.

[15] Christoph Friedrich, Mathias C. Müller, and Stefan Blügel. Erratum: Band convergence and linearization error correction of all-electron *GW* calculations: The extreme case of zinc oxide [phys. rev. b 83, 081101(r) (2011)]. *Phys. Rev. B*, 84(3):039906, Jul 2011.

[16] M. Stankovski, G. Antonius, D. Waroquiers, A. Miglio, H. Dixit, K. Sankaran, M. Giantomassi, X. Gonze, M. Côté, and G.-M. Rignanese. G^0W^0 band gap of zno: Effects of plasmon-pole models. *Phys. Rev. B*, 84:241201(R), Dec 2011.

[17] Stefan Albrecht, Lucia Reining, Rodolfo Del Sole, and Giovanni Onida. *Ab Initio* calculation of excitonic effects in the optical spectra of semiconductors. *Phys. Rev. Lett.*, 80:4510–4513, May 1998.

[18] Lorin X. Benedict, Eric L. Shirley, and Robert B. Bohn. Theory of optical absorption in diamond, si, ge, and gaas. *Phys. Rev. B*, 57:R9385–R9387, Apr 1998.

[19] Michael Rohlfing and Steven G. Louie. Electron-hole excitations in semiconductors and insulators. *Phys. Rev. Lett.*, 81:2312–2315, Sep 1998.

[20] Giovanni Onida, Lucia Reining, and Angel Rubio. Electronic excitations: density-functional versus many-body green's-function approaches. *Rev. Mod. Phys.*, 74:601–659, Jun 2002.

[21] A. Zangwill and Paul Soven. Density-functional approach to local-field effects in finite systems: Photoabsorption in the rare gases. *Phys. Rev. A*, 21:1561, 1980.

[22] P. L. de Boeij, F. Kootstra, J. A. Berger, R. van Leeuwen, and J. G. Snijders. Current density functional theory for optical spectra: A polarization functional. *J. Chem. Phys.*, 115(5):1995–1999, 2001.

[23] Lucia Reining, Valerio Olevano, Angel Rubio, and Giovanni Onida. Excitonic effects in solids described by time-dependent density-functional theory. *Phys. Rev. Lett.*, 88:066404, Jan 2002.

[24] Silvana Botti, Francesco Sottile, Nathalie Vast, Valerio Olevano, Lucia Reining, Hans-Christian Weissker, Angel Rubio, Giovanni Onida, Rodolfo Del Sole, and R. W. Godby. Long-range contribution to the exchange-correlation kernel of time-dependent density functional theory. *Phys. Rev. B*, 69:155112, Apr 2004.

[25] Francesco Sottile, Valerio Olevano, and Lucia Reining. Parameter-free calculation of response functions in time-dependent density-functional theory. *Phys. Rev. Lett.*, 91:056402, Jul 2003.

[26] Andrea Marini, Rodolfo Del Sole, and Angel Rubio. Bound excitons in time-dependent density-functional theory: Optical and energy-loss spectra. *Phys. Rev. Lett.*, 91:256402, Dec 2003.

[27] Gianni Adragna, Rodolfo Del Sole, and Andrea Marini. *Ab initio* calculation of the exchange-correlation kernel in extended systems. *Phys. Rev. B*, 68:165108, Oct 2003.

[28] R. Stubner, I. V. Tokatly, and O. Pankratov. Excitonic effects in time-dependent density-functional theory: an analytically solvable model. *Phys. Rev. B*, 70:245119, Dec 2004.

[29] Ulf von Barth, Nils Erik Dahlen, Robert van Leeuwen, and Gianluca Stefanucci. Conserving approximations in time-dependent density functional theory. *Phys. Rev. B*, 72:235109, Dec 2005.

[30] G. Vignale and Walter Kohn. Current-dependent exchange-correlation potential for dynamical linear response theory. *Phys. Rev. Lett.*, 77:2037–2040, Sep 1996.

[31] J. A. Berger, P. L. de Boeij, and R. van Leeuwen. Analysis of the viscoelastic coefficients in the vignale-kohn functional: The cases of one- and three-dimensional polyacetylene. *Phys. Rev. B*, 71:155104, Apr 2005.

[32] J. A. Berger, P. Romaniello, R. van Leeuwen, and P. L. de Boeij. Performance of the vignale-kohn functional in the linear response of metals. *Phys. Rev. B*, 74:245117, Dec 2006.

[33] J. A. Berger, P. L. de Boeij, and R. van Leeuwen. Analysis of the vignale-kohn current functional in the calculation of the optical spectra of semiconductors. *Phys. Rev. B*, 75:035116, Jan 2007.

[34] S. Sharma, J. K. Dewhurst, A. Sanna, and E. K. U. Gross. Bootstrap approximation for the exchange-correlation kernel of time-dependent density-functional theory. *Phys. Rev. Lett.*, 107:186401, Oct 2011.

[35] Santiago Rigamonti, Silvana Botti, Valérie Veniard, Claudia Draxl, Lucia Reining, and Francesco Sottile. Estimating excitonic effects in the absorption spectra of solids: Problems and insight from a guided iteration scheme. *Phys. Rev. Lett.*, 114:146402, Apr 2015.

[36] S. Sharma, J. K. Dewhurst, A. Sanna, and E. K. U. Gross. Comment on "estimating excitonic effects in the absorption spectra of solids: Problems and insight from a guided iteration scheme". *Phys. Rev. Lett.*, 117:159701, Oct 2016.

[37] Santiago Rigamonti, Silvana Botti, Valérie Veniard, Claudia Draxl, Lucia Reining, and Francesco Sottile. Rigamonti et al. reply:. *Phys. Rev. Lett.*, 117:159702, Oct 2016.

[38] Adrian Stan, Pina Romaniello, Santiago Rigamonti, Lucia Reining, and J A Berger. Unphysical and physical solutions in many-body theories: from weak to strong correlation. *New J. Phys.*, 17(9):093045, 2015.

[39] V. U. Nazarov and G. Vignale. Optics of semiconductors from meta-generalized-gradient-approximation-based time-dependent density-functional theory. *Phys. Rev. Lett.*, 107:216402, Nov 2011.

[40] Paolo E. Trevisanutto, Aleksandrs Terentjevs, Lucian A. Constantin, Valerio Olevano, and Fabio Della Sala. Optical spectra of solids obtained by time-dependent density functional theory with the jellium-with-gap-model exchange-correlation kernel. *Phys. Rev. B*, 87:205143, May 2013.

[41] Zeng-hui Yang, Francesco Sottile, and Carsten A. Ullrich. Simple screened exact-exchange approach for excitonic properties in solids. *Phys. Rev. B*, 92:035202, Jul 2015.

[42] Sivan Refaely-Abramson, Manish Jain, Sahar Sharifzadeh, Jeffrey B. Neaton, and Leeor Kronik. Solid-state optical absorption from optimally tuned time-dependent range-separated hybrid density functional theory. *Phys. Rev. B*, 92:081204, Aug 2015.

[43] J. A. Berger. Fully parameter-free calculation of optical spectra for insulators, semiconductors, and metals from a simple polarization functional. *Phys. Rev. Lett.*, 115:137402, Sep 2015.

[44] F. Kootstra, P. L. de Boeij, and J. G. Snijders. Efficient real-space approach to time-dependent density functional theory for the dielectric response of nonmetallic crystals. *J. Chem. Phys.*, 112(15):6517–6531, 2000.

[45] Silvana Botti, Armel Fourreau, F Nguyen, Yves-Olivier Renault, Francesco Sottile, and Lucia Reining. Energy dependence of the exchange-correlation kernel

of time-dependent density functional theory: A simple model for solids. *Phys. Rev. B*, 72:125203, Sep 2005.

[46] V. Saile, M. Skibowski, W. Steinmann, P. Gürtler, E. E. Koch, and A. Kozevnikov. Observation of surface excitons in rare-gas solids. *Phys. Rev. Lett.*, 37:305–308, Aug 1976.

[47] D. M. Roessler and W. C. Walker. *J. Opt. Soc. Am.*, 57:835, 1967.

[48] P. Lautenschlager, M. Garriga, L. Vina, and M. Cardona. Temperature dependence of the dielectric function and interband critical points in silicon. *Phys. Rev. B*, 36:4821–4830, Sep 1987.

[49] Stefan Zollner, Miquel Garriga, Jens Kircher, Josef Humlíček, Manuel Cardona, and Georg Neuhold. Temperature dependence of the dielectric function and the interband critical-point parameters of gap. *Phys. Rev. B*, 48:7915–7929, Sep 1993.

[50] H. R. Phillip and E. A. Taft. Kramers-kronig analysis of reflectance data for diamond. *Phys. Rev.*, 136:A1445–A1448, Nov 1964.

[51] K. Stahrenberg, Th. Herrmann, K. Wilmers, N. Esser, W. Richter, and M. J. G. Lee. Optical properties of copper and silver in the energy range 2.5˘9.0 ev. *Phys. Rev. B*, 64:115111, Aug 2001.

[52] H. J. Hagemann, W. Gudat, and C. Kunz. *J. Opt. Soc. Am.*, 65:742, 1975.

[53] Nathaniel Raimbault, Paul L. de Boeij, Pina Romaniello, and J. A. Berger. Gauge-invariant calculation of static and dynamical magnetic properties from the current density. *Phys. Rev. Lett.*, 114:066404, Feb 2015.

[54] G Strinati. Application of the greens functions method to the study of the optical properties of semiconductors. *Nuovo Cimento*, 11(12):1–86, december 1988.

[55] D.P. Chong. Augmenting basis set for time-dependent density functional theory calculation of excitation energies: Slater-type orbitals for hydrogen to krypton. *Mol. Phys.*, 103(6-8):749–761, 2005.

[56] E. I. Tellgren, A. M. Teale, J. W. Furness, K. K. Lange, U. Ekström, and T. Helgaker. Non-perturbative calculation of molecular magnetic properties within current-density functional theory. *J. Chem. Phys.*, 140(3):034101, 2014.

[57] David P. Lide, editor. *CRC Handbook of Chemistry and Physics*. CRC PRESS, 81 edition, 2000.

[58] C. Barter, R. G. Meisenheimer, and D. P. Stevenson. Diamagnetic susceptibilities of simple hydrocarbons and volatile hydrides. *J. Phys. Chem.*, 64(9):1312–1316, 1960.

[59] B. Zuniga-Gutierrez, G. Geudtner, and A. M. Köster. Magnetizability tensors from auxiliary density functional theory. *J. Chem. Phys.*, 137:094113–1, September 2012.

[60] Geoffrey L.D. Ritchie and Jonathan N. Watson. Temperature dependence of electric field-gradient induced birefringence (the buckingham effect) in {C6H6} and c6f6: comparison of electric and magnetic properties of {C6H6} and {C6F6}. *Chem. Phys. Lett.*, 322(34):143 – 148, 2000.

[61] A. Pacault. *Bull. Soc. Chim. Fr.*, 16:D371, 1949.

[62] M. Carnell, S.D. Peyerimhoff, A. Breest, K.H. Gdderz, P. Ochmann, and J. Hormes. Experimental and quantum-theoretical investigation of the circular dichroism spectrum of r-methyloxirane. *Chem. Phys. Lett.*, 180(5):477 – 481, 1991.

[63] A Breest, P Ochmann, F Pulm, KH Gödderz, M Carnell, and J Hormes. Experimental circular-dichroism and vuv spectra of substituted oxiranes and thiiranes. *Mol. Phys.*, 82(3):539–551, JUN 20 1994.

[64] M. G. Mason and O. Schnepp. Absorption and circular dichroism spectra of ethylenic chromophorestranscyclooctene, and pinene. *J. Chem. Phys.*, 59(3):1092–1098, 1973.

[65] Jochen Autschbach, Serguei Patchkovskii, Tom Ziegler, Stan J. A. van Gisbergen, and Evert Jan Baerends. Chiroptical properties from time-dependent density functional theory. ii. optical rotations of small to medium sized organic molecules. *J. Chem. Phys.*, 117(2):581–592, 2002.

[66] Yoshiyuki Kumata, Junji Furukawa, and Takayuki Fueno. The effect of solvents on the optical rotation of poly(propylene oxide). *Bull. Chem. Soc. Jpn*, 43(12):3663–3666, 1970.

[67] Volker Schurig, Bernhard Koppenhoefer, and Waldemar Buerkle. Preparation and determination of configurationally pure trans-(2s,3s)-2,3-epoxybutane. *J. Org. Chem.*, 45(3):538–541, 1980.

[68] G.K. Helmkamp and N. Schnautz. Stereochemistry of the lithium aluminum deuteride reduction of the thiirane ring. *Tetrahedron*, 2(3-4):304–307, may 1958.

[69] R. Rossi and P. Diversi. Synthesis, absolute configuration, optical purity and spectral properties of optically active 3-methylcyclobutene. *Tetrahedron*, 26(21):5033 – 5039, 1970.

[70] William R. Moore, Howard W. Anderson, Stephen D. Clark, and Thomas M. Ozretich. Absolute configuration of (+)-1,2-cyclononadiene. *J. Am. Chem. Soc.*, 93(19):4932–4934, 1971.

[71] Herbert C. Brown, Prabhakar K. Jadhav, and Manoj C. Desai. A convenient procedure for upgrading commercial (+)- and (-)-.alpha.-pinene to material of high optical purity. *J. Org. Chem.*, 47(23):4583–4584, 1982.

[72] Hans Jrgen Bestmann and Wolfgang Both. Molekle mit helixstruktur, i. synthese und absolute konfiguration des (+)-pentahelicens. *Chem. Ber.*, 107(9):2923–2925, 1974.

[73] A.L. Fetter and J. D. Walecka. *Quantum Theory of Many-Particle Systems.* Dover publications, 2003.

[74] J. M. Luttinger and J. C. Ward. Ground-state energy of a many-fermion system. ii. *Phys. Rev.*, 118:1417–1427, Jun 1960.

[75] Giovanna Lani, Pina Romaniello, and Lucia Reining. Approximations for many-body green's functions: insights from the fundamental equations. *New J. Phys.*, 14(1):013056, 2012.

[76] F. Tandetzky, J. K. Dewhurst, S. Sharma, and E. K. U. Gross. *arXiv:1205.4274.*, 2012.

[77] Hideo Fukutome. Theory of the unrestricted hartree-fock equation and its solutions. i. *Prog. Theor. Phys.*, 45(5):1382–1406, 1971.

[78] Rolf Seeger and John A. Pople. Selfconsistent molecular orbital methods. xviii. constraints and stability in hartreefock theory. *J. Chem. Phys.*, 66(7):3045–3050, 1977.

[79] Rdiger Bauernschmitt and Reinhart Ahlrichs. Stability analysis for solutions of the closed shell kohnsham equation. *J. Chem. Phys.*, 104(22):9047–9052, 1996.

[80] Alex J. W. Thom and Martin Head-Gordon. Locating multiple self-consistent field solutions: An approach inspired by metadynamics. *Phys. Rev. Lett.*, 101:193001, Nov 2008.

[81] L. G. Molinari. Hedin's equations and enumeration of feynman diagrams. *Phys. Rev. B*, 71:113102, Mar 2005.

[82] L. G. Molinari and N. Manini. Enumeration of many-body skeleton diagrams. *Eur. Phys. J. B*, 51(3):331–336, 2006.

[83] Y. Pavlyukh and W. Hübner. Analytic solution of hedin's equations in zero dimensions. *J. Math. Phys.*, 48(5):052109, 2007.

[84] J A Berger, Pina Romaniello, Falk Tandetzky, Bernardo S Mendoza, Christian Brouder, and Lucia Reining. Solution to the many-body problem in one point. *New J. Phys.*, 16(11):113025, 2014.

[85] P. C. Martin and J. Schwinger. Theory of many-particle systems. I. *Phys. Rev.*, 115:1342–1373, 1959.

[86] R. Chitra and Gabriel Kotliar. Effective-action approach to strongly correlated fermion systems. *Phys. Rev. B*, 63:115110, Mar 2001.

[87] M Potthoff. Effective-action approach to strongly correlated fermion systems. *Condensed Matter Physics*, 9:557, 2006.

[88] P. E. Blöchl, T. Pruschke, and M. Potthoff. *Phys. Rev. B*, 88:205139, 2013.

[89] Evgeny Kozik, Michel Ferrero, and Antoine Georges. Nonexistence of the luttinger-ward functional and misleading convergence of skeleton diagrammatic series for hubbard-like models. *Phys. Rev. Lett.*, 114:156402, Apr 2015.

[90] T. Schäfer, G. Rohringer, O. Gunnarsson, S. Ciuchi, G. Sangiovanni, and A. Toschi. Divergent precursors of the mott-hubbard transition at the two-particle level. *Phys. Rev. Lett.*, 110:246405, Jun 2013.

[91] M. Potthoff. Self-energy-functional approach to systems of correlated electrons. *Eur. Phys. J. B*, 32(4):429–436, 2003.

[92] R. Eder. *arXiv:1407.6599*, 2014.

[93] T. Thonhauser, Davide Ceresoli, David Vanderbilt, and R. Resta. Orbital magnetization in periodic insulators. *Phys. Rev. Lett.*, 95:137205, Sep 2005.

[94] Di Xiao, Yugui Yao, Zhong Fang, and Qian Niu. Berry-phase effect in anomalous thermoelectric transport. *Phys. Rev. Lett.*, 97:026603, Jul 2006.

[95] Junren Shi, G. Vignale, Di Xiao, and Qian Niu. Quantum theory of orbital magnetization and its generalization to interacting systems. *Phys. Rev. Lett.*, 99:197202, Nov 2007.

[96] Raffaello Bianco and Raffaele Resta. Orbital magnetization as a local property. *Phys. Rev. Lett.*, 110:087202, Feb 2013.

[97] F. Aryasetiawan, K. Karlsson, and T. Miyake. Green's function theory of orbital magnetic moment of interacting electrons in solids. *Phys. Rev. B*, 93:161104, Apr 2016.

[98] D. Hsieh, D. Qian, L. Wray, Y. Xia, Y. S. Hor, R. J. Cava, and M. Z. Hasan. A topological dirac insulator in a quantum spin hall phase. *Nature*, 452(7190):970–974, 2008.

[99] Y. Tanaka, Zhi Ren, T. Sato, K. Nakayama, S. Souma, T. Takahashi, Kouji Segawa, and Yoichi Ando. Experimental realization of a topological crystalline insulator in snte. *Nat Phys*, 8(11):800–803, 11 2012.

[100] Frank Wilczek. Two applications of axion electrodynamics. *Phys. Rev. Lett.*, 58:1799–1802, May 1987.

[101] Ming-Che Chang and Min-Fong Yang. Optical signature of topological insulators. *Phys. Rev. B*, 80:113304, Sep 2009.

[102] Jun ichi Inoue. An optical test for identifying topological insulator thin films. *Opt. Express*, 21(7):8564–8569, Apr 2013.

[103] J. Vidal, X. Zhang, L. Yu, J.-W. Luo, and A. Zunger. False-positive and false-negative assignments of topological insulators in density functional theory and hybrids. *Phys. Rev. B*, 84:041109, Jul 2011.

[104] Xiao-Liang Qi, Taylor L. Hughes, and Shou-Cheng Zhang. Topological field theory of time-reversal invariant insulators. *Phys. Rev. B*, 78:195424, Nov 2008.

[105] Andrew M. Essin, Joel E. Moore, and David Vanderbilt. Magnetoelectric polarizability and axion electrodynamics in crystalline insulators. *Phys. Rev. Lett.*, 102:146805, Apr 2009.

[106] Liang Fu, C. L. Kane, and E. J. Mele. Topological insulators in three dimensions. *Phys. Rev. Lett.*, 98:106803, Mar 2007.

[107] Luuk J. P. Ament, Michel van Veenendaal, Thomas P. Devereaux, John P. Hill, and Jeroen van den Brink. Resonant inelastic x-ray scattering studies of elementary excitations. *Rev. Mod. Phys.*, 83:705–767, Jun 2011.

[108] Masatoshi Imada, Atsushi Fujimori, and Yoshinori Tokura. Metal-insulator transitions. *Rev. Mod. Phys.*, 70:1039–1263, Oct 1998.

[109] J. H. Shim, K. Haule, and G. Kotliar. Fluctuating valence in a correlated solid and the anomalous properties of [dgr]-plutonium. *Nature*, 446(7135):513–516, 2007.

[110] J. Georg Bednorz and K. Alex Müller. Perovskite-type oxides¯the new approach to high-T_c superconductivity. *Rev. Mod. Phys.*, 60:585–600, Jul 1988.

[111] R. von Helmolt, J. Wecker, B. Holzapfel, L. Schultz, and K. Samwer. Giant negative magnetoresistance in perovskitelike $la_{2/3}ba_{1/3}mno_x$ ferromagnetic films. *Phys. Rev. Lett.*, 71:2331–2333, Oct 1993.

[112] S. Jin, T. H. Tiefel, M. McCormack, R. A. Fastnacht, R. Ramesh, and L. H. Chen. Thousandfold change in resistivity in magnetoresistive la-ca-mn-o films. 264(5157):413–415, 1994.

[113] Stefano Di Sabatino, J. A. Berger, Lucia Reining, and Pina Romaniello. Photoemission spectra from reduced density matrices: The band gap in strongly correlated systems. *Phys. Rev. B*, 94:155141, Oct 2016.

[114] E. Papalazarou, Matteo Gatti, M. Marsi, V. Brouet, F. Iori, Lucia Reining, E. Annese, I. Vobornik, F. Offi, A. Fondacaro, S. Huotari, P. Lacovig, O. Tjernberg, N. B. Brookes, M. Sacchi, P. Metcalf, and G. Panaccione. Valence-band electronic structure of V_2O_3: Identification of v and o bands. *Phys. Rev. B*, 80:155115, Oct 2009.